The Astrophysical Journal, 872:167 (21pp), 2019 February 20 https://doi.org/10.3847/1538-4357/ab0206

MACER Improved: AGN Feedback Computed in Rotating Early-type Galaxies at High Resolution

Zhaoming Gan[1], Luca Ciotti[2], Jeremiah P. Ostriker[3], and Feng Yuan[1]
[1] Shanghai Astronomical Observatory, Chinese Academy of Sciences, 80 Nandan Road, Shanghai 200030, People's Republic of China
[2] Department of Physics and Astronomy, University of Bologna, via Piero Gobetti 93/2, I-40129 Bologna, Italy
[3] Department of Astronomy, Columbia University, 550 W. 120th Street, New York, NY 10027, USA
Received 2018 September 11; revised 2019 January 22; accepted 2019 January 24; published 2019 February 20

Abstract

Based on our previous modeling of active galactic nucleus (AGN) feedback in isolated elliptical galaxies using the MACER (Massive AGN Controlled Ellipticals Resolved) code, we extend and improve the model to include rotation, to facilitate angular momentum transfer via the Toomre instability in gaseous disks, to limit the star formation to regions of high density and low temperature, and to improve the treatment of hot-mode (low accretion rate) AGN feedback. The model galaxy now has an extended dark matter profile that matches with standard observations, but it has a resolution of parsecs in the inner region and resolves the Bondi radius. We find that the results agree reasonably well with a panoply of observations: (1) Both AGN activity and star formation are primarily in central cold gaseous disks, are bursty, and are mainly driven by the Toomre instability. (2) The AGN duty cycle agrees well with the Soltan argument, i.e., the AGN spends most of its lifetime when it is in low luminosity (half of the time with $L/L_{\rm Edd} < 7 \times 10^{-5}$), while emitting most of its energy when it is in high luminosity (half of radiant energy emitted with $L/L_{\rm Edd} > 0.06$). (3) The total star formation is roughly a few percent of the initial stellar mass, occurring in the bursts that would be associated with the observed E+A phenomenon. Most of the star formation occurs in a circumnuclear disk of size $\leqslant$1 kpc, which is in agreement with recent observations. (4) The interstellar medium X-ray luminosity varies within a reasonable range (median $L_{\rm X,ISM} = 9.1 \times 10^{39}$ erg s^{-1}), in agreement with observations.

Key words: black hole physics – galaxies: elliptical and lenticular, cD – galaxies: evolution – methods: numerical

1. Introduction

Most of the stellar mass seen in the universe is in relatively massive elliptical galaxies (Drory et al. 2009) which apparently form at relatively high redshift as "blue nuggets," become quiescent "red nuggets" at intermediate redshift (van Dokkum et al. 2015), and accumulate an outer envelope of accreted low-mass, low-metallicity stars at late times (Naab et al. 2007; Greene et al. 2009). Subsequent episodes of star formation and "E+A" phases contribute ∼2% more stars during this interval. The literature has been recently reviewed by Somerville & Davé (2015) and Naab & Ostriker (2017). The overall two-phase evolution was outlined by Oser et al. (2010), with the role of active galactic nucleus (AGN) feedback in quenching star formation discussed by many authors (e.g., Di Matteo et al. 2005; Springel et al. 2005; Cattaneo & Teyssier 2007; Ciotti & Ostriker 2007; Booth & Schaye 2009; Dubois et al. 2010, 2013; Ostriker et al. 2010; Debuhr et al. 2011; Novak et al. 2011; Choi et al. 2012; Fabian 2012; Gaspari et al. 2012; Hirschmann et al. 2014; Crain et al. 2015; Sijacki et al. 2015; Eisenreich et al. 2017; Hopkins et al. 2018; Tremmel et al. 2019; Weinberger et al. 2018; Yuan et al. 2018).

Thus, for most of the observable lifetime ($z < 2$) these systems have an evolution largely driven by internal processes. The primary source of mass addition (∼15% of the stellar mass) is from normal stellar evolution, while the primary energy and momentum feedback is from Type Ia supernovae (SNe Ia) and central supermassive black holes with a sporadically important SN II input (important after bursts of star formation). Cosmological codes, which are necessary during the formation phase, are ill suited to explore the physics of this second phase, due to their low spatial resolution and consequent inability to model the inner several hundred parsecs within which AGN feeding and feedback are determined and which provide the sites for starburst episodes and inner disk formation.

Over some time we have developed a high-resolution mesh code to address this phase of galaxy evolution. The first paper in this series is Ciotti & Ostriker (1997). With over 20 papers in the series, we have named the steadily improving code "MACER" for Massive AGN Controlled Ellipticals Resolved, and this paper outlines several of the recent substantial code improvements now available to treat the complex evolution of elliptical galaxies. The code has high spatial resolution (parsecs in the inner regions), standard and relatively complete stellar physics and chemical evolution, and implementation of AGN feedback that is designed to match observed BAL winds and luminous output for high accretion rates and a new physically modeled mode (Yuan et al. 2015) for the low accretion (hot) outflows. Radiative transfer is included in a simplified, spherical Eddington approximation fashion. The purpose of this paper is to add some essential improvements to the physical modeling, to determine the consequences of these changes, and to propose observational tests that will help to ascertain the accuracy of the improved treatments.

In brief, we find that in even moderately rotating normal ellipticals there will be periodic formation of central, cool gas disks that will become unstable to the classic Toomre instability (Toomre 1964) leading to both starbursts and AGN feeding/feedback.

2. Model Setup

To study black hole feeding and feedback, we need to answer two fundamental questions: (i) what are the mass

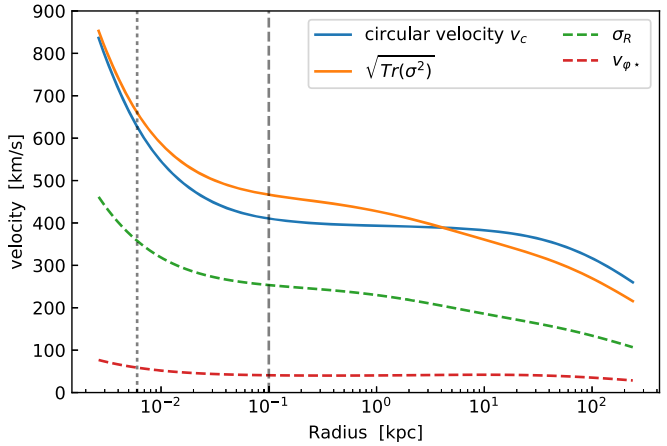

Figure 1. Characteristic velocities (on the equatorial plane, i.e., $\theta = \pi/2$) of the model galaxy: (1) circular velocity (v_c, which characterizes the total gravitational potential; blue line); (2) square root of the trace of stellar velocity dispersion ($\sqrt{\mathrm{Tr}(\sigma^2)}$, which determines the stellar thermalization; orange line); (3) radial stellar velocity dispersion (σ_R; green dashed line); and (4) the ordered rotation velocity of stars ($v_{\varphi\star}$, which determines the specific angular momentum of the stellar mass loss; red dashed line). The galaxy model parameters adopted are $M_\star = 3.35 \times 10^{11}\,M_\odot$, $r_\star = 9.3$ kpc, $\mathcal{R} = 20$, $\xi = 20$, $\mu = 10^{-3}$, $\eta = 0.2$, and $k = 0.25$. The vertical dotted line shows approximately the Bondi radius (∼6 pc, assuming a typical ISM temperature of 10^7 K). The vertical dashed line shows approximately the radius of influence of the black hole (∼100 pc). The inner boundary of our simulations is 2.5 pc.

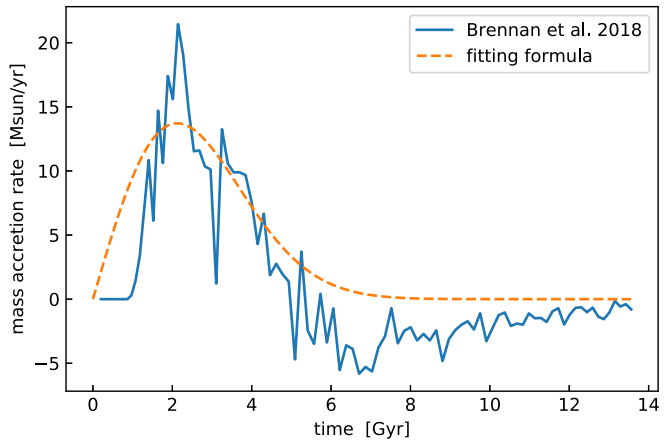

Figure 2. Mass accretion rate of the CGM infalling onto the galaxy outskirt. The net mass accretion profile (blue solid line) is adopted from a large cosmological zoom simulation by Brennan et al. (2018). In our simulations, we use the fitting formula (Equation (12); orange dashed line) with total accreted mass being 8.3% of the initial stellar mass.

sources, and (ii) how is the mass transported to the galaxy center? Apparently, the mass sources could be (1) the remnant interstellar medium (ISM) from the galaxy formation; (2) mass accretion onto the galaxy (e.g., from the cosmic web); (3) stellar mass loss (e.g., stellar winds from AGBs); and (4) recycled gas from the AGNs (e.g., BAL winds, ultrafast outflows, hot disk winds, etc.) and both SNe I and SNe II. Provided sufficient mass supply, the ISM could be supported by thermal pressure and/or rotation (angular momentum) against the gravity, which prevents the ISM from being accreted too rapidly by the central supermassive black hole. It has been known for decades that there is nominally a strong "cooling flow problem" (Fabian 1994): the gas observed via X-rays in normal massive ellipticals has a radiative cooling time quite short compared to the Hubble time. There are energy sources available based on both the central supermassive black holes and normal stellar feedback that could balance these losses, but determining the quasi-equilibrium requires a delicate treatment of both energy inputs and outputs since we know empirically that there are periodic collapses of cool gas to the center, occurring when energy input does not balance radiative losses, that result in AGN outbursts, star formation episodes, and the resultant "E+A" phenomenon (Dressler & Gunn 1982).

Previous papers in this series found that a slowly varying quasi-equilibrium typically exists with gas input primarily from the AGB phase of late stellar evolution of the low-mass stars approximately balanced by mass outflows driven by SNe Ia (see early work by Renzini et al. 1993). This quasi-equilibrium is punctuated by episodes of cooling flow accompanied with star formation and black hole accretion that in turn produce violent AGN activities and blow out gas into the circumgalactic medium (CGM).

In this paper we will show how these processes are modified by the addition of rotation (see also Yoon et al. 2018), a more massive halo, and a better algorithm for the star formation. We will find that the overall character of the evolution remains (quasi-equilibrium interrupted by outbursts), but the geometry is changed significantly by the periodic formations of cool, dense, Toomre-unstable central disks of approximately kiloparsec size within which most of the regulatory activity occurs. In principle, star formation could be efficient enough to consume the ISM before it would be accreted by the supermassive black hole. Hence, it is important to treat all of the processes properly in a self-consistent model, and it is prone to be a large-dynamical-range problem. It is our aim in this paper to consider all the processes above in one single high-resolution hydrodynamical simulation, taking the galaxy as a "background" and tracking the fluid dynamics of the galactic medium during a cosmological timescale. In the rest of this section, we organize the context according to the physics we add in. First of all, the evolution of the galactic medium is governed by the following time-dependent Eulerian hydrodynamic equations:

$$\frac{\partial \rho}{\partial t} + \nabla \cdot (\rho \boldsymbol{v}) = -\nabla \cdot \dot{\boldsymbol{m}}_Q + \dot{\rho}_{\rm II} + \dot{\rho}_{\rm I} + \dot{\rho}_\star - \dot{\rho}_\star^+, \quad (1)$$

$$\frac{\partial \boldsymbol{m}}{\partial t} + \nabla \cdot (\boldsymbol{m}\boldsymbol{v}) = -\nabla p_{\rm gas} - \nabla p_{\rm rad} - \rho \nabla \phi - \nabla \cdot \Pi_{\rm vis} - \nabla \cdot \Pi_Q + \dot{\boldsymbol{m}}_{\rm S} - \dot{\boldsymbol{m}}_\star^+, \quad (2)$$

$$\frac{\partial E}{\partial t} + \nabla \cdot (E\boldsymbol{v}) = -p_{\rm gas} \nabla \cdot \boldsymbol{v} - \Pi_{\rm vis} : \nabla \boldsymbol{v} + H - C + \dot{E}_{\rm Q} + \dot{E}_{\rm II} + \dot{E}_{\rm I} + \dot{E}_{\rm S} - \dot{E}_\star^+, \quad (3)$$

where ρ, $\boldsymbol{m}$, E, $p_{\rm gas}$, and $\boldsymbol{v}$ are the fluid density, momentum, internal energy, thermal pressure, and velocity, respectively. Here $p_{\rm rad}$ is the radiation pressure of AGN irradiation due to both scattering $(\nabla p_{\rm rad})_{\rm es}$ and absorption $(\nabla p_{\rm rad})_{\rm abs}$ (Section 2.7, Equation (33)). The adiabatic index is fixed to $\gamma = 5/3$. $\phi = \phi_{\rm g} + \phi_{\rm BH}$ is the total gravitational potential of the galaxy (stars + dark matter [DM]) $\phi_{\rm g}$, plus that of the central supermassive black hole of mass $M_{\rm BH}$, $\phi_{\rm BH} = -GM_{\rm BH}/r$. The self-gravity of the gas is not taken into account (see Section 2.1 for more details).

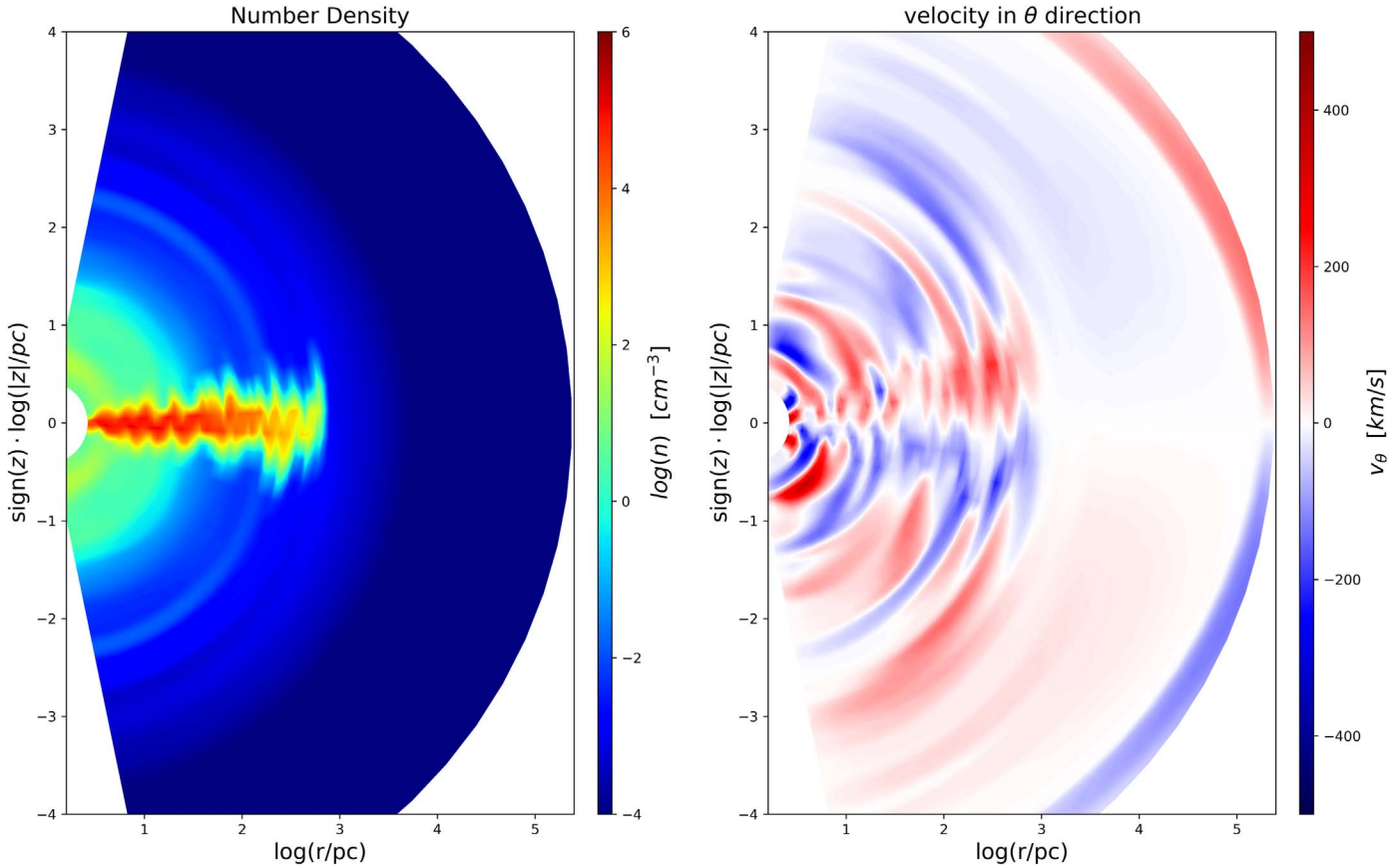

Figure 3. Circumnuclear disk formed in the fiducial run (at the end of the simulation). Left panel: pseudo-color map of the ISM number density (which is wiggling). Right panel: pseudo-color map of the azimuthal velocity v_θ (the ISM near the equatorial plane is collapsing onto the disk). The cold dense inner disk has a radius of several hundred parsecs. Note the logarithmic radial scale.

Regarding the mass sources, we treat the remnant ISM as the initial condition (Section 2.8) and treat the mass accretion onto the galaxy (CGM infall in our case; see Section 2.3) as outer boundary conditions, so they do not explicitly appear in the equations above. Our estimate for CGM infall is taken from the full cosmological zoom simulations (Choi et al. 2017; Brennan et al. 2018). Besides, the stellar passive evolution is treated as source terms (Section 2.2), including the mass sources and energy heating contributed by AGBs ($\dot{\rho}_\star$, $\dot{E}_{\rm S}$), SNe Ia ($\dot{\rho}_{\rm I}$, $\dot{E}_{\rm I}$), and SNe II ($\dot{\rho}_{\rm II}$, $\dot{E}_{\rm II}$), and also the momentum source term $\dot{\boldsymbol{m}}_{\rm S}$, since the stellar mass loss above would inherit the stream velocity (e.g., rotation, if any; Equation (9)) of its host stars (please see Appendix B for an outline, and we refer the readers to Ciotti & Ostriker 2012 for a full description). We also take into account active stellar evolution, where $\dot{\rho}_\star^+$, $\dot{\boldsymbol{m}}_\star^+$, and $\dot{E}_\star^+$ are the mass, momentum, and energy sink terms, respectively, associated with star formation (Section 2.6).

It is known that SNe Ia alone are capable of heating the ISM up to the local virial temperature. The hot gas cannot be accreted efficiently because of its thermal pressure gradient and low density, so it is extremely important to evaluate the energy gain/loss of the ISM. In the energy equation above, H and C are the net radiative heating and cooling (under AGN irradiation), respectively, which include Compton heating/cooling, bremsstrahlung cooling, and line heating (photoionization)/cooling (recombination). We refer the readers to Sazonov et al. (2005) for more details (see also Novak et al. 2011; Ciotti & Ostriker 2012); a brief highlight is also presented in Appendix A for the completeness of this paper. We note that it falls back automatically to the case of the passive (atomic) cooling when the AGN luminosity is zero.

In the cases with rotation, the ISM with high angular momentum would naturally cool, condense, and form a circumnuclear disk. The ISM on the disk cannot be accreted without losing its angular momentum, and it will be consumed by star formation eventually, for example, Eisenreich et al. (2017) found in their SPH simulations that circumnuclear disks commonly form in the galaxy centers, and intensive star formation occurs within those gaseous cold disks. As proposed by Hopkins & Quataert (2010, 2011), one of the most promising mechanisms for angular momentum transfer on the galactic scale is the gravitational torque due to nonaxisymmetric structures of the stellar population (see also Lodato 2008 and references therein). We assume axisymmetry in our galaxy model (see Section 2.1), so we do not include the Hopkins & Quataert mechanism for self-consistency (however, see Yoon et al. 2018 for an alternative treatment). However, if the gaseous disk is dense enough to become locally self-gravitating, it is prone to be gravitationally unstable (Toomre 1964). In this paper, we propose a numerical algorithm for such gravitational instability, in which we treat it as a diffusive process, where $\dot{E}_Q$, Π_Q, and $\dot{\boldsymbol{m}}_Q$ count for the energy dissipation, angular momentum transfer, and mass transport, respectively, due to the Toomre instability (Section 2.4). Besides, we also use the "α prescription" ($\Pi_{\rm vis}$; see Section 2.5) to mimic the magnetorotational instability

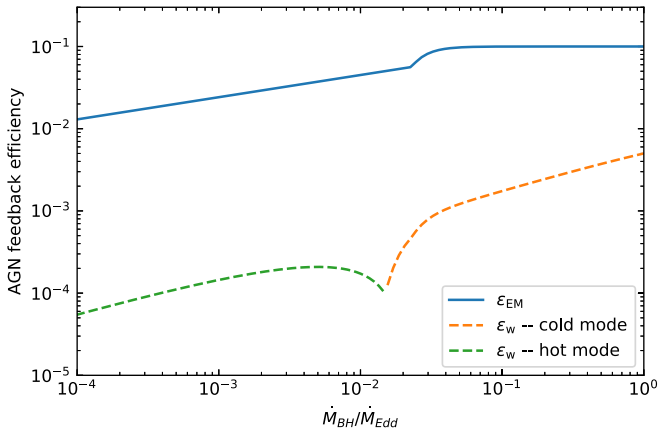

Figure 4. Radiative efficiency (blue sold line) and wind efficiency (dashed lines) adopted in our two-mode AGN feedback (subgrid) model. The mode transitions at $\dot{M}_{\rm BH} \simeq 0.02\dot{M}_{\rm Edd}$ (see, e.g., Yuan & Narayan 2014). Both curves are designed to approximately match observed feedback efficiencies.

(MRI; Balbus & Hawley 1998) in the disk, which can also transfer angular momentum.

AGN mechanical feedback (in terms of disk winds) is treated as inner boundary conditions, similar to the CGM infall, i.e., injecting wind mass/momentum/energy at the inner boundary (note that AGN radiation feedback is already included in the heating and cooling function *H–C* as per earlier papers in this series; see Section 2.7 for a detailed description).

Finally, we utilize the `Athena++` code (version 1.0.0; Stone et al. 2008) to solve the hydrodynamical equations above. The `Athena++` code is a state-of-art, grid-based radiation magneto-hydrodynamical code. It has flexible coordinate and grid options, e.g., including spherical coordinates combined with adaptive mesh refinement, which make it ideal for large-dynamical-range simulations like those we have made in this paper. Particularly, we use spherical coordinates assuming axisymmetry while allowing rotation (aka 2.5-dimensional simulation). The outer boundary is chosen as 250 kpc to enclose the whole massive elliptical galaxy, whereas the inner boundary is set to be 2.5 pc to resolve the Bondi radius so that we are able to self-consistently track the black hole feeding processes. We use a logarithmic grid ($\Delta r_{\rm i+1}/\Delta r_{\rm i} = 1.1$) to divide the radial axis into 120 discrete cells. We subtract two small conical zones near the poles to avoid the well-known axial numerical singularity; the azimuthal angle θ is divided into 30 uniform cells and covers an azimuthal range from 0.05π to 0.95π. The numerical solver for the gas dynamics is composed by the combination of the HLLE Riemann solver, the PLM reconstruction, and the second-order van Leer integrator.

2.1. Structure and Dynamics of the Galaxy Models

As is well known, the structural and dynamical properties of the galaxies are one of the main factors determining the gas evolution in early-type galaxies (ETGs). In this paper we focus on the effects of large-scale ordered rotation; the adopted models are constructed accordingly. All the necessary steps needed in the construction of an axisymmetric rotating ETG (such as the determination of the structural parameters, the amount and distribution of DM, the recovery of the galaxy gravitational potential and force field, and the solution of the Jeans equations) can be found elsewhere (Posacki et al. 2013; Negri et al. 2014a, 2014b, and in particular in Negri et al. 2015; Ciotti et al. 2017; Pellegrini et al. 2018), so we do not repeat here. In particular, in these works the galaxy models were constructed by solving numerically the Poisson and the two-integrals Jeans equations.

Here, instead, we use a different approach, adopting fully analytical axisymmetric models obtained by homeoidal expansion (Ciotti & Bertin 2005) of the two-component JJ spherical models discussed in Ciotti & Ziaee Lorzad (2018, hereafter CZ18). Ellipsoidal JJ models are made by the superposition of a Jaffe (1983) stellar ellipsoidal density distribution added to a DM halo so that the *total* density distribution is another ellipsoidal Jaffe model, in general with different flattening and scale length. For a thorough discussion of the structural and dynamical properties of these models see L. Ciotti & A. Ziaee Lorzad (2019, in preparation, hereafter CZ19).

The advantage of this approach is that it is very easy to change galaxy parameters (an important aspect in exploratory works) and to implement the relevant physical formulae in the hydrodynamical code. At the same time, the models agree with the main observational properties of ETGs (a stellar density distribution closely following the de Vaucouleurs empirical law over a large range, a DM halo well approximated by the Navarro–Frenk–White (NFW) formula, adjustable flattening in the stellar component and in the total mass distribution, a parameterized amount of ordered rotation, allowing for the construction of galaxy models spanning the cases from tangential anisotropy to isotropic rotators, etc). In addition, these models in the case of moderate flattening (say, for galaxies rounder than *E*4) allow for the analytical solution of the Jeans equations for the stellar component also in the presence of a central black hole. Note that, with the Jeans equations being linear in the potentials, this allows us in turn to update at each time step the values of the rotational velocity and of the velocity dispersion tensor due to an increasing mass of the central black hole. We also notice that one could also change, as a function of time, the DM halo concentration, to explore the effects of halo contraction/expansion and black hole growth on the gas flows.

The density distribution is described by an oblate Jaffe (1983) model of axial ratio $q_\star$, total mass $M_\star$, and scale length $r_\star$:

$$\rho_\star = \frac{M_\star}{4\pi r_\star^3}\frac{1}{q_\star m^2(1+m)^2}, \quad m^2 = s^2\left(\sin^2\theta + \frac{\cos^2\theta}{q_\star^2}\right), \quad (4)$$

where $s \equiv r/r_\star$ and (r, θ, φ) are the standard spherical coordinates. In spherical models ($q_\star = 1$), $R_{\rm e} \simeq 0.75\, r_\star$, where $R_{\rm e}$ is the effective radius of the galaxy; in the edge-on projection of oblate models, $R_{\rm e} \simeq 0.75\sqrt{q_\star}\, r_\star$.

In JJ models we then assign the total galaxy density (stars + DM) $\rho_{\rm g}$, so that the resulting DM halo is given by the difference $\rho_{\rm g} - \rho_\star$. Here for simplicity we restrict to the case of a spherical total density $\rho_{\rm g}$, given by a spherical Jaffe profile of total mass $M_{\rm g} = \mathcal{R}M_\star$ and scale length $r_{\rm g} = \xi r_\star$, so that

$$\rho_{\rm g} = \frac{M_\star}{4\pi r_\star^3}\frac{\mathcal{R}\xi}{s^2(\xi+s)^2}. \quad (5)$$

The positivity request of $\rho_{\rm g}$ imposes constraints on the values of $\mathcal{R}$ and ξ, and in CZ18 it is shown that in the *minimum halo*

models (as those used here) the DM profile is described very well by the NFW profile.

The total gravitational potential of the galaxy plus the central massive black hole (MBH) of mass $M_{\rm BH} = \mu M_\star$ is then given by

$$\phi = \phi_{\rm g} + \phi_{\rm BH} = \frac{GM_\star \mathcal{R}}{r_\star \xi} \ln\left(\frac{s}{s+\xi}\right) - \frac{GM_\star \mu}{r_\star s}. \quad (6)$$

The circular velocity in the equatorial plane is given by

$$\frac{v_c^2}{r} = \frac{d\phi}{dr}. \quad (7)$$

In CZ19 the Jeans equations are solved, and it shows that the radial and vertical velocity dispersions, $\sigma_R = \sigma_z$, can be written as

$$\rho_\star \times \sigma_R^2 = \frac{GM_\star^2}{4\pi r_\star^4} \times \left\{ \mu[A(s) + \eta B(s) + \eta C(s) s^2 \sin^2\theta] + \frac{\mathcal{R}}{\xi}[D(\xi, s) + \eta E(\xi, s) + \eta F(\xi, s) s^2 \sin^2\theta] \right\}, \quad (8)$$

where $\eta = 1 - q_\star$ and the radial function are simple analytical functions, and the separate contributions of the central MBH and of the galaxy potential to the velocity dispersion are apparent. For spherical JJ models, the central projected velocity dispersion of stars, due to the galaxy contribution only, is given by $\sigma_{\rm p}^2(0) = GM_\star \mathcal{R}/(2r_\star \xi)$, and this is a very good approximation also for the ellipsoidal models for low flattening.

As is well known, the two-integral Jeans equations are degenerate, i.e., they just provide the total (ordered plus velocity dispersion) kinetic energy in the azimuthal direction, via the quantity $\Delta_\star = v_{\varphi\star}^2 + \sigma_\varphi^2 - \sigma_R^2$, where $v_{\varphi\star}$ is the ordered (i.e., streaming) velocity field of stars. To break the degeneracy, we adopt the usual Satoh (1980) decomposition (even though more complicated decompositions could be used; see, e.g., Ciotti & Pellegrini 1996; Negri et al. 2014a), with

$$v_{\varphi\star}^2 = k^2 \Delta_\star. \quad (9)$$

In CZ19 it is shown that for the present models

$$\rho_\star \times \Delta_\star = \frac{GM_\star^2 \eta\, s^2 \sin^2\theta}{2\pi r_\star^4} \times \left[\mu\, C(s) + \frac{\mathcal{R}\, F(\xi, s)}{\xi}\right]; \quad (10)$$

the explicit form of the radial functions $A - F$ is given in CZ19. Finally, we can obtain the trace of the velocity as

$$\mathrm{Tr}(\sigma^2) = 3\sigma_R^2 + (1 - k^2)\Delta_\star. \quad (11)$$

With the ordered and dispersive velocity field, we are able to evaluate the specific angular momentum and also the stellar thermalization (see Appendix B for details). In the fiducial setup, we study a massive rotating elliptical galaxy with total stellar mass $M_\star = 3.35 \times 10^{11}\, M_\odot$ (assuming a mass-to-light ratio of 5.8 in the solar unit, scale radius $r_\star = 9.3$ kpc, $\mathcal{R} = 20$, $\xi = 20$, $\eta = 0.2$, and $k = 0.25$). The resulting estimate for the central projected velocity dispersion of stars (without the black hole contribution) is therefore $\simeq 280\ \mathrm{km\ s^{-1}}$, placing the galaxy model on the observed scaling laws of ETGs. The initial black hole mass $M_{\rm BH}$ is set to $3.35 \times 10^8\, M_\odot$ (i.e., $\mu = 10^{-3}$; Magorrian et al. 1998; Kormendy & Ho 2013). In Figure 1, we plot the velocity profiles (on the equatorial plane, i.e., $\theta = \pi/2$) derived from the total gravitational potential.

2.2. Stellar Feedback

The model galaxy is assumed to be 2 Gyr old at the beginning of our simulations, and we track the ISM dynamics for a time span of 12 Gyr. During such a period, the total stellar mass loss is ∼10% of the initial stellar mass, which alone is far more than enough to fuel the central supermassive black hole. We consider both SN Ia feedback from the old stellar population and SN II feedback from the newly formed stars during the simulations, as they are important energy sources to heat the ISM. Of course, we need an initial mass function (IMF) to evaluate the overall stellar evolution, and we adopt the Salpeter profile.

Numerically, we treat the stellar feedback as source terms, i.e., inject the mass in situ where it is produced, and assume that it inherits the velocity of its host stars (Ho 2009). Apparently, the kinetic energy due to the velocity dispersion would be quickly thermalized (aka stellar thermalization), and the ISM could be heated to a temperature nearly equal to the local virial temperature. The angular momentum (ordered rotating velocity field) should be conserved (see Appendix B for details).

2.3. CGM Infall

It is known that the mass accretion from the cosmic web can be very significant when compared to the ISM content remaining in the galaxies. We adopt the gas accretion profile onto the elliptical galaxies in cosmological zoom-in simulations from Brennan et al. (2018). We take the mean accretion rate of 30 central elliptical galaxies, with mean stellar mass of $2 \times 10^{11}\, M\odot$ at $z = 0$ (Choi et al. 2017). In Figure 2 we show the normalized mass accretion rate versus time. In our numerical setup, we fit the profile as follows:

$$\dot{M}_{\rm CGM} = \frac{M_{\rm acc}}{t_0/2 \cdot [1 - e^{-(\Delta t/t_0)^2}]} \cdot (t/t_0) \cdot e^{-(t/t_0)^2}, \quad (12)$$

where $t_0 = 3$ Gyr and $M_{\rm acc}$ is the total mass accreted during the time span of $\Delta t = 12$ Gyr. We scale $M_{\rm acc}$ according to the total stellar mass of the modeling galaxy (see below for details), and we can see that the CGM infall occurs mainly in the early epoch when $t < 6$ Gyr.

Numerically, we inject the CGM at the outer boundary of the computational domain, which can be considered as a boundary condition. The injected CGM is assumed to be nearly freefall (with a constant $v_r = -(2/3)v_c$ and zero rotation velocity over the boundary at $r = 250$ kpc). Its sound speed is assumed to be $c_s^2 = (5/9)v_c^2$. The parameters above are chosen to make sure that the infalling gas is bound to the galaxy gravity. The CGM inflow flux is weighted by $\sin^2(\theta)$, i.e., most of the CGM is injected near the equatorial plane. The total mass infall is scaled according to the stellar mass $M_\star$, and it is taken to be $M_{\rm acc} = 2.8 \times 10^{10}\, M_\odot (= 8.3\% M_\star)$, which is comparable to the total stellar mass loss and approximately two times the mass of the initial ISM (Section 2.8).

2.4. Circumnuclear Disk and Toomre Instability

As ISM accumulates in the galaxy from the stellar mass loss and/or the CGM infall, it would be subject to a cooling flow.

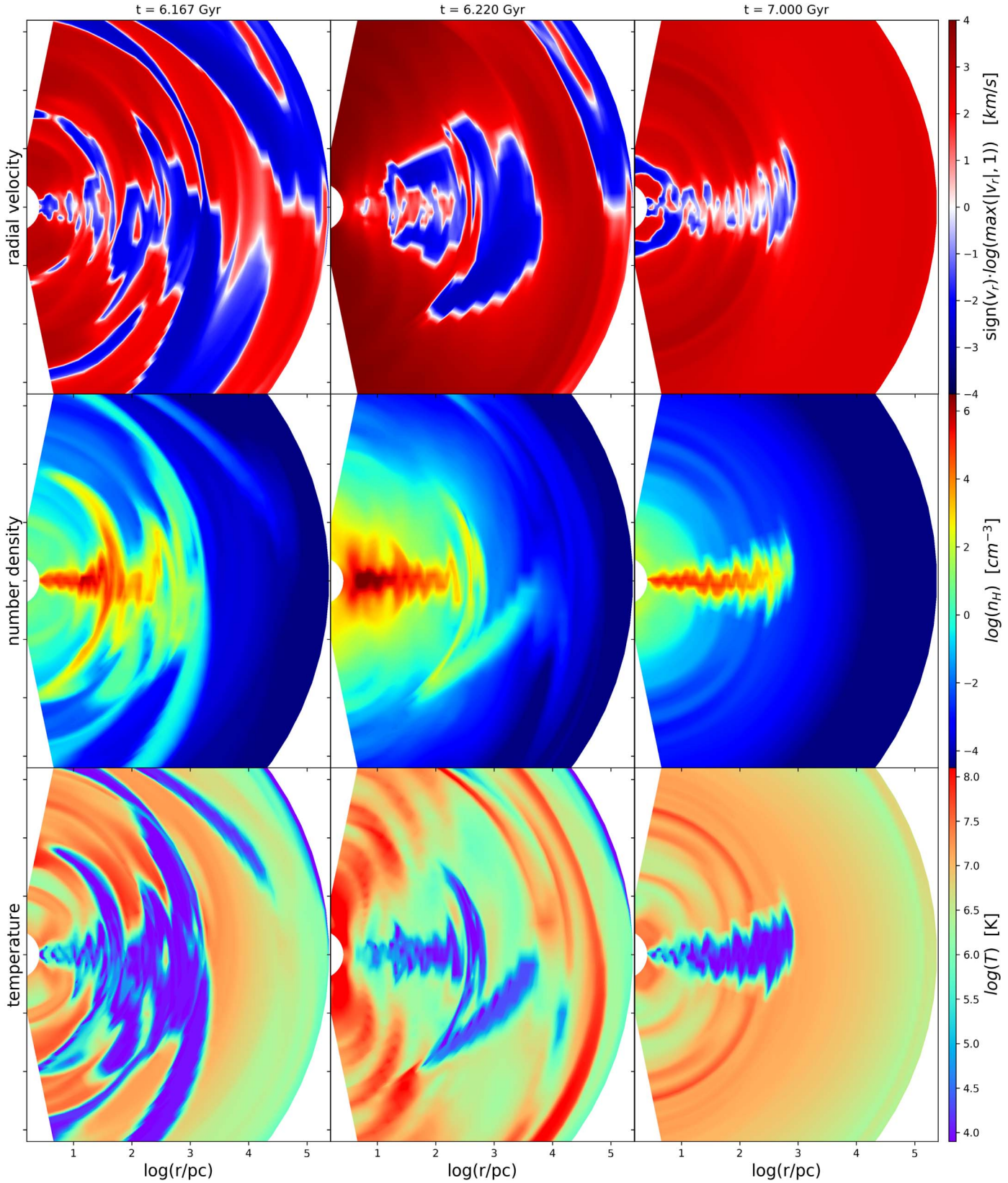

Figure 5. Hydrodynamical properties of the circumnuclear disk during an AGN/star formation burst. From top to bottom, it shows the radial velocity (outflow in red, inflow in blue), number density, and temperature, respectively. From left to right, it shows the results at $t = 6.167$ Gyr (just before the burst), $t = 6.22$ Gyr (during the burst), and $t = 7.0$ Gyr (after the burst), respectively. Note the standing shocks due to infalling gas above/below the cool central disks.

When the ISM cools down via radiation cooling, a cold disk forms because of the angular momentum barrier (as shown in Figure 3). SAURON and ATLAS have reported on the observations of cold gaseous disks in over half of the observed ellipticals (Sarzi et al. 2006; Davis et al. 2011; see also Boizelle et al. 2017 for ALMA observations). It is well known that such

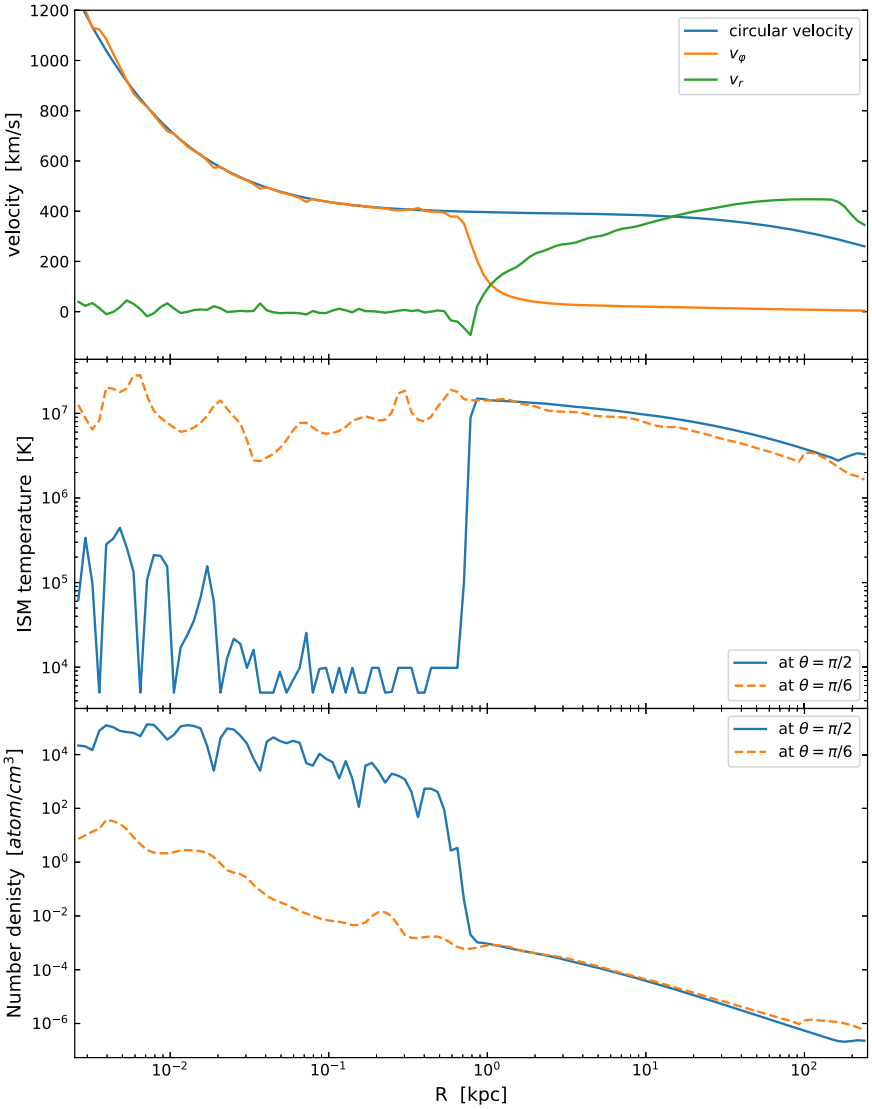

Figure 6. Circularization of the circumnuclear disk. The ISM velocity, temperature, and density profiles on ($\theta = \pi/2$; solid lines) and off ($\theta = \pi/6$; dashed lines) the disk (at $t = 12$ Gyr) are shown in the top, middle, and bottom panels, respectively. The ISM in the circumnuclear disk simply hits the temperature floor, and it is solely supported by rotation against gravity.

a cold dense disk can become gravitationally unstable if its surface density is greater than some critical value (aka the Toomre instability). The Toomre criterion considers that the disk is unstable (Toomre 1964) when

$$Q \equiv \frac{c_s \kappa}{\pi G \Sigma} < 1, \tag{13}$$

where Σ is the surface density of the disk and κ is the local epicyclic frequency,

$$\kappa^2 \equiv \frac{2\Omega}{r}\frac{d(r^2\Omega)}{dr}, \quad \text{where} \quad \Omega = \frac{v_c}{r}. \tag{14}$$

As a consequence of the gravitational instability, spiral waves will be developed in the cold disk, which are capable of *transferring angular momentum outward* by virtue of the nonaxisymmetric gravitational torque and at the same time *transferring mass inward*. The typical timescale is around the local orbital time. However, limited by our two-dimensional settings, we take in account the effect of the Toomre instability by proposing a semianalytical algorithm, while we leave solving the self-gravity of the gas in a full three-dimensional simulation to our future work. To mimic such a process of angular momentum transfer, we propose a numerical algorithm as follows:

1. We sample the disk density vertically (as the cold disk is geometrically thin, we sample along the θ direction for simplicity). Then, we could evaluate the disk surface density and finally determine the Toomre Q parameter of each disk ring.
2. When a disk ring becomes unstable ($Q < 1$), we move the ring inward at the rate below and calculate the mass flux ($\dot{\boldsymbol{m}}_Q$) accordingly:

$$\frac{dr}{dt} = \frac{\Delta Q \cdot r}{\pi r / v_c}, \quad \text{where} \quad \Delta Q = \max(1 - Q, 0). \tag{15}$$

3. We assume that the gas inherits the temperature and velocity of the inner adjacent ring. To conserve angular momentum, we dispose of the excessive angular momentum (Π_Q) in the outer adjacent ring. To conserve energy, we dissipate the thermal energy gain $\dot{E}_Q$ into the inner, local, and outer rings according to a partition of

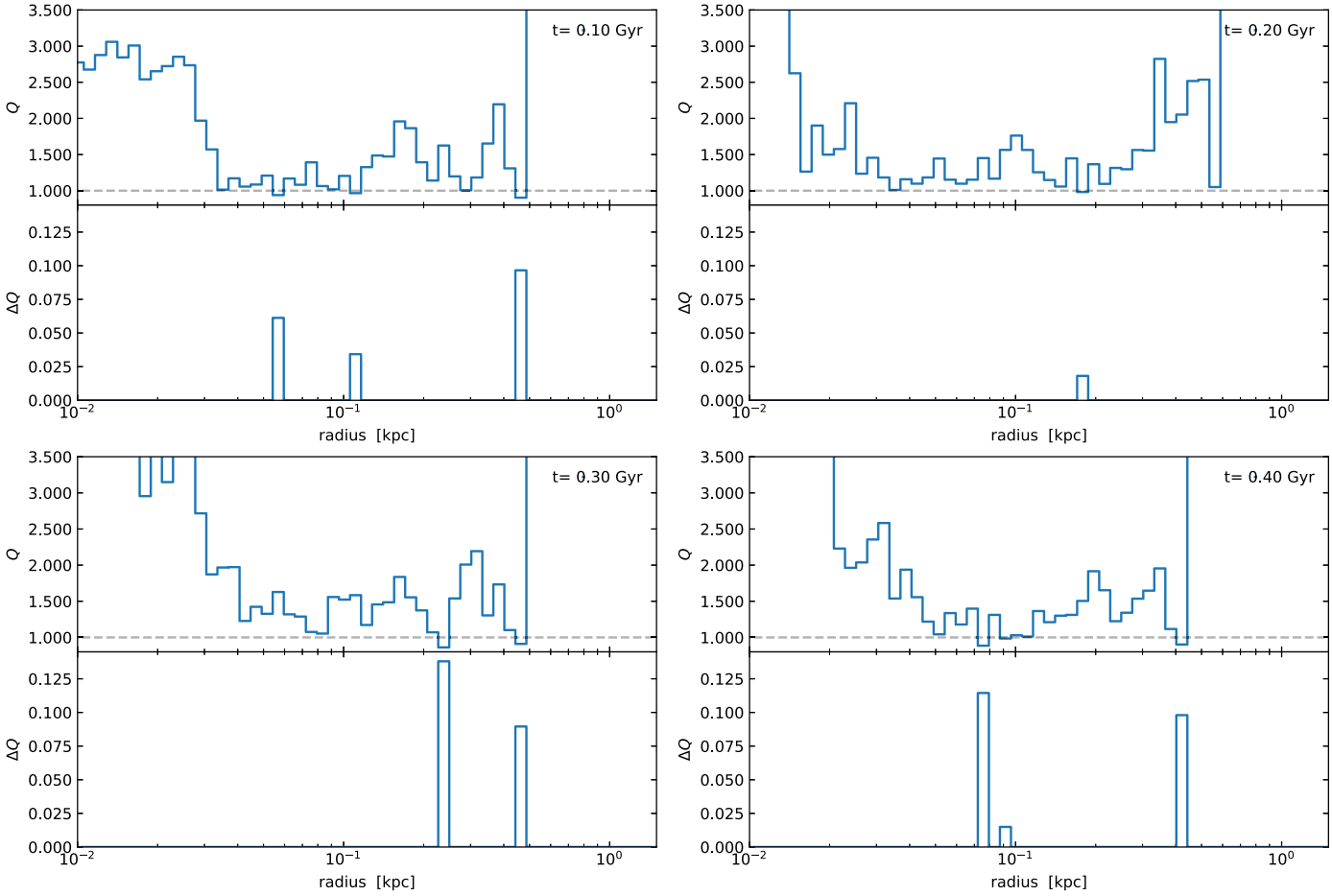

Figure 7. Toomre Q parameter. In the four panels, we plot the results on the equatorial plane at a selection of representative times, i.e., $t = 0.1$, 0.2, 0.3, and 0.4 Gyr, respectively. In each panel, we show the Toomre Q parameter in the upper subplot and $\Delta Q \equiv \max(1 - Q, 0)$ in the lower subplot. We can see that the Toomre instability occurs in individual disk rings.

1/4, 1/2, and 1/4, respectively. So, locally the angular momentum and mass transfer rates are proportional to ΔQ, and mass/angular momentum/energy are all conserved.

2.5. Viscosity in the Circumnuclear Disk

As in black hole accretion disks, there should also be an effective viscosity in the circumnuclear disk due to the MRI (Balbus & Hawley 1998). To count in the magnetic process in our hydrodynamic simulations, we use the "α prescription" (Shakura & Sunyaev 1973) to mimic the MRI effects in transferring angular momentum (e.g., Takasao et al. 2018; Zhu & Stone 2018). The viscosity coefficient reads

$$\nu = \alpha \cdot c_s^2/\Omega, \tag{16}$$

where c_s is the sound speed as usual. To confine the viscous effects to within the circumnuclear disk, we propose a profile of the dimensionless viscosity parameter α as follows:

$$\alpha = \alpha_0 \cdot \exp\left[-3\left(\frac{v_\varphi - v_c}{v_\varphi}\right)^2\right], \tag{17}$$

where (v_φ, v_c) are the actual and circular rotational velocities of the gas, respectively. We adopt $\alpha_0 = 0.03$ as indicated by magnetohydrodynamical simulations (Zhu & Stone 2018), i.e., α is constant within the rotation-supported disk, while it decays rapidly if it is off the disk. Following Stone et al. (1999), we assume that the azimuthal components of the viscous shear tensor $\Pi_{\rm vis}$ are nonzero, i.e.,

$$\Pi_{{\rm vis},r\varphi} = -\rho\nu \cdot \frac{\partial}{\partial r}\left(\frac{v_\varphi}{r}\right), \tag{18}$$

$$\Pi_{{\rm vis},\theta\varphi} = -\rho\nu \cdot \frac{\sin\theta}{r}\frac{\partial}{\partial\theta}\left(\frac{v_\varphi}{\sin\theta}\right). \tag{19}$$

From the equations above, we can see that the ratio between the viscosity timescale $\tau_{\rm vis}$ and the local orbital timescale $\tau_{\rm rot}$ scales approximately as $\tau_{\rm vis}/\tau_{\rm rot} \propto (1/\alpha)(v_\varphi/c_s)^2$. As the temperature of the cold circumnuclear disk is far below the local virial temperature, i.e., $c_s \ll v_c \sim v_\varphi$, the viscosity timescale is usually much longer than $\tau_{\rm rot}$. Recalling that the timescale of the Toomre instability is comparable to $\tau_{\rm rot}$ (see Equation (15)), the angular momentum transfer is thus usually dominated by the Toomre instability in our model setup if parts of the disk are dense enough to become gravitationally unstable.

The angular momentum transfer mechanisms above make it possible for the gas in the circumnuclear disks to be accreted by the central supermassive black hole and to trigger AGN activities.

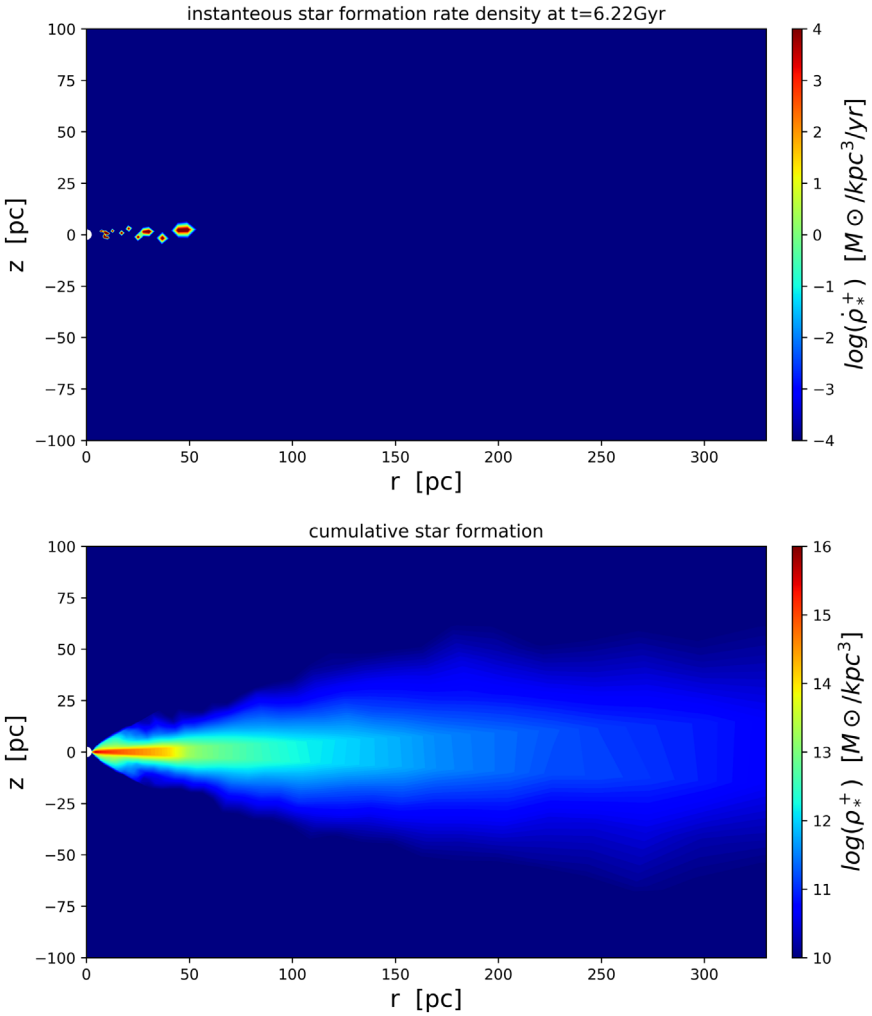

Figure 8. Spatial distribution of star formation. Top panel: instantaneous star formation rate density in our fiducial at $t = 6.22$ Gyr (instantaneous star formation occurs in individual disk rings). Bottom panel: cumulative star formation at the end of the simulation (most of star formation occurs in the cold disk).

2.6. Star Formation

Another consequence of gravitational instability is star formation, i.e., when the ISM cools down and becomes dense enough, it is subject to the Jeans instability and would trigger star formation. However, it is also known that rotation would somehow stabilize the flow and suppress star formation. Similarly, we propose the star formation rate in the disk as follows when it is Toomre unstable:

$$\begin{aligned}\dot{\rho}^{+}_{\star,Q} &= \eta_{\rm SF,Q}\cdot\Delta Q\cdot\rho\cdot\Omega \\ &= \eta_{\rm SF,Q}\cdot\Delta Q\cdot\rho\cdot\sqrt{4\pi G\bar{\rho}/3}\,,\end{aligned} \tag{20}$$

where $\bar{\rho}$ is the mean density interior to the radius. We assume $\eta_{\rm SF,Q} = 0.1$. When turning gas into stars, we simply subtract the amount of gas with the in situ fluid velocity and temperature and replace it with stars without changing the specific energy and momentum per unit mass,

$$\dot{\boldsymbol{m}}^{+}_{\star,Q} = \frac{\dot{\rho}^{+}_{\star,Q}}{\rho}\cdot\boldsymbol{m},\quad \dot{E}^{+}_{\star,Q} = \frac{\dot{\rho}^{+}_{\star,Q}}{\rho}\cdot E. \tag{21}$$

Throughout the galaxy we also evaluate the star formation due to the local Jeans instability (though it is suppressed by rotation). More specifically (Ciotti & Ostriker 2012),

$$\dot{\rho}^{+}_{\star,C} = \frac{\eta_{\rm SF,C}\rho}{\tau_{\rm SF,C}},\quad \dot{\boldsymbol{m}}^{+}_{\star,C} = \frac{\eta_{\rm SF,C}\boldsymbol{m}}{\tau_{\rm SF,C}},\quad \dot{E}^{+}_{\star,C} = \frac{\eta_{\rm SF,C}E}{\tau_{\rm SF,C}}. \tag{22}$$

We set a low star formation efficiency $\eta_{\rm SF,C} = 0.01$ and $\tau_{\rm SF,C} = \max(\tau_{\rm cool}, \tau_{\rm dyn})$, where

$$\tau_{\rm cool} = \frac{E}{C},\quad \tau_{\rm dyn} = \min(\tau_{\rm Jeans}, \tau_{\rm rot}). \tag{23}$$

In addition, we do not allow star formation when the gas density is lower than 10^5 atoms cm^{-3} or when the gas temperature is higher than 4×10^4 K. Although we do not include the formation of molecular gas, our very high threshold for star formation, which is possible, given our high resolution, is comparable to the density in star-forming molecular clouds.

The total star formation rate is the sum of Equations (20) and (22),

$$\begin{aligned}&\dot{\rho}^{+}_{\star} = \dot{\rho}^{+}_{\star,Q} + \dot{\rho}^{+}_{\star,C},\quad \dot{\boldsymbol{m}}^{+}_{\star} = \dot{\boldsymbol{m}}^{+}_{\star,Q} + \dot{\boldsymbol{m}}^{+}_{\star,C},\\ &\dot{E}^{+}_{\star} = \dot{E}^{+}_{\star,Q} + \dot{E}^{+}_{\star,C}.\end{aligned} \tag{24}$$

The cold circumnuclear disk is the fuel reservoir for both star formation and black hole accretion, and there is a tough

competition between these two processes. For example, if star formation is very efficient, most (if not all) of the cold gas will be consumed before it could be accreted by the supermassive black hole, so the AGN activities will be significantly suppressed. Vice versa, if angular moment transfer is very efficient, strong AGN feedback will be triggered, which in turn will suppress star formation further. However, both star formation and angular momentum transfer are related to the same physics, which means that they are of similar timescales, i.e., the timescale of the Toomre instability. It would be very interesting to study the balance between the two important processes.

2.7. AGN Feedback

Our model for AGN feedback is founded on the concept that we should model the physics as closely as possible on the observed electromagnetic and wind outputs. AGN radiation feedback interacts with the system by affecting the radiation source terms *H–C*. AGN wind feedback is implemented by injecting wind mass, momentum, and energy via the inner boundary directly, so it does not implicitly appear in the equations above. In the numerical setup, radiation feedback is determined by the AGN luminosity $L_{\rm BH}$ and its Compton (radiation) temperature $T_{\rm X}$, while wind feedback is characterized by the wind mass loading rate $\dot{M}_w$ and its velocity v_w, which are determined by the AGN subgrid model below (we refer the readers to Ostriker et al. 2010 and Yuan et al. 2018 for more details). Note that we do not yet include the feedback effect of collimated jets. We leave it to our future work, as the underlying physics of jet feedback on the galaxy scale is still an important open question (see, e.g., Nesvadba et al. 2006, 2007, 2017; Salomé et al. 2006; Guo & Oh 2008; Tortora et al. 2009; Wagner et al. 2012; Hitomi Collaboration 2016; Yang & Reynolds 2016; Zhuravleva et al. 2016; Fabian et al. 2017). For completeness of this paper, we briefly introduce the model setup and highlight the improvement we have made.

By solving the time-dependent Eulerian equations (Equations (1)–(3)), we can track the mass inflow across the inner boundary, which would fall into the galaxy center (after a timescale $\tau_{\rm infall} \sim 3 \times 10^3$ yr—from the inner boundary to the black hole accretion disk) and eventually form a black hole accretion disk (assuming a disk size of 2000 $GM_{\rm BH}/c^2$, which gives an accretion timescale of ∼800 yr—from the disk to the black hole horizon). After considering the time lags above, we obtain the disk accretion rate $\dot{M}_{\rm disk}$, based on which ($\dot{M}_{\rm disk} = \dot{M}_{\rm BH} + \dot{M}_w$) we finally evaluate the black hole accretion rate $\dot{M}_{\rm BH}$ (so $L_{\rm BH}$, $T_{\rm X}$) and also the nuclear wind properties ($\dot{M}_w$, v_w) according to our knowledge of black hole accretion theory and observed outflows.

We use the two-mode black hole accretion scenario (Yuan et al. 2018) to achieve closure of the subgrid model, which gives the relation between $\dot{M}_{\rm BH}$ and $\dot{M}_w$: (1) when the mass supply is sufficient, it will result in a relatively large value for $\dot{M}_{\rm disk}$, i.e., the density within the accretion disk could be high enough to make it radiatively efficient (Shakura & Sunyaev 1973), and then it should be in the cold (quasar) mode; (2) otherwise, it is in the hot mode, i.e., the radiatively inefficient mode but with strong wind (i.e., mass outflow; see, e.g., Stone et al. 1999; Narayan et al. 2012; Yuan et al. 2012, 2015; Li et al. 2013). In the simulations, we switch the AGN subgrid model between the cold and hot modes according to a critical disk accretion rate $\dot{M}_{\rm disk,crit} = 0.02\dot{M}_{\rm Edd}$ (where $\dot{M}_{\rm Edd} \equiv L_{\rm Edd}/0.1c^2$ and $L_{\rm Edd}$ is the Eddington luminosity; see Yuan & Narayan 2014 and references therein). That is, when $\dot{M}_{\rm disk} \geqslant \dot{M}_{\rm disk,crit}$, we set it to the cold mode; otherwise, we switch it to the hot mode.

Following the notations in Ostriker et al. (2010), the AGN wind energy and momentum can be written as functions of its mass loading rate $\dot{M}_w$ and the wind velocity v_w,

$$\dot{E}_w = \frac{1}{2}\dot{M}_w v_w^2 \equiv \epsilon_w \dot{M}_{\rm BH} c^2, \quad \dot{P}_w = \dot{M}_w v_w. \tag{25}$$

In the cold (high accretion rate) mode, we assume a constant wind velocity of 10^4 km s^{-1}, while allowing the wind feedback efficiency ϵ_w to vary as a function of the dimensionless AGN luminosity l with a characteristic value of $\epsilon_w^M = 5 \times 10^{-3}$ (as in Ostriker et al. 2010), i.e.,

$$\dot{M}_w = \frac{2\epsilon_w \dot{M}_{\rm BH} c^2}{v_w^2}, \quad v_w = 10^4 \ {\rm km\ s^{-1}}, \tag{26}$$

where

$$\epsilon_w = \epsilon_w^M \sqrt{\frac{5}{4} \cdot \frac{l}{1 + l/4} \cdot e^{-(\dot{M}_{\rm disk,crit}/\dot{M}_{\rm BH})^4}}, \quad l \equiv \frac{L_{\rm BH}}{L_{\rm Edd}}. \tag{27}$$

This is estimated to roughly match observations of BAL outflows (Arav et al. 1994, 2008).

In the hot (low accretion rate) mode, the wind mass loading rate and the wind velocity are determined by the "truncation" radius $r_{\rm tr}$ (i.e., the outer boundary of the hot accretion disk; Yuan et al. 2015):

$$\dot{M}_w = \dot{M}_{\rm disk} \cdot \left(1 - \sqrt{\frac{3r_s}{r_{\rm tr}}}\right), \quad v_w = 0.1\sqrt{\frac{GM_{\rm BH}}{r_{\rm tr}}}, \tag{28}$$

where $r_s = 2\ GM_{\rm BH}/c^2$ and

$$r_{\rm tr} = 3r_s \left(\frac{\dot{M}_{\rm disk,crit}}{\dot{M}_{\rm disk}}\right)^2. \tag{29}$$

By solving the AGN subgrid model above, we could get $\dot{M}_w$, $\dot{P}_w$, $\dot{E}_w$, and $\dot{M}_{\rm BH}$. Then, we translate $\dot{M}_{\rm BH}$ to the AGN luminosity $L_{\rm BH}$ by assuming the radiation efficiency $\epsilon_{\rm EM}$ as follows (Xie & Yuan 2012; see Figure 4):

$$L_{\rm BH} = \epsilon_{\rm EM} \dot{M}_{\rm BH} c^2 \equiv \epsilon_{\rm EM} \cdot \dot{m} \cdot L_{\rm Edd}/0.1, \tag{30}$$

where

$$\epsilon_{\rm EM} = \begin{cases} 0.100 \times e^{-(\dot{M}_{\rm disk,crit}/\dot{M}_{\rm BH})^4}, & \dot{m} > 2.3 \times 10^{-2}; \\ 0.045 \times \left(\dfrac{\dot{m}}{0.01}\right)^{0.27}, & 2.3 \times 10^{-2} > \dot{m} > 9.4 \times 10^{-5}; \\ 0.200 \times \left(\dfrac{\dot{m}}{0.01}\right)^{0.59}, & \dot{m} < 9.4 \times 10^{-5}. \end{cases} \tag{31}$$

Given the AGN luminosity, we set the Compton temperature $T_{\rm X}$ as follows (see Equation (36); Sazonov et al. 2005; Xie et al. 2017):

$$T_{\rm X} = \begin{cases} 2.5 \times 10^7 \ {\rm K}, & l > 0.02; \\ 1.0 \times 10^8 \ {\rm K}, & l \leqslant 0.02. \end{cases} \tag{32}$$

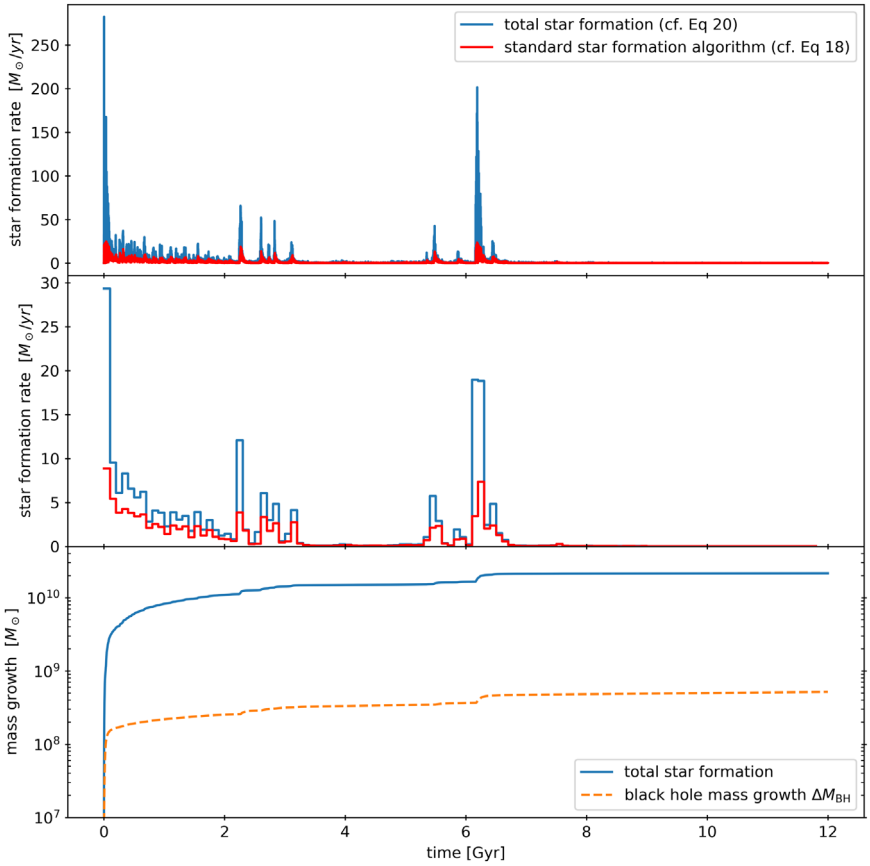

Figure 9. Total star formation integrated over the whole galaxy. Top panel: star formation rate vs. time; Middle panel: same as the top panel, except that the data points are binned and averaged over equal time intervals of $\Delta t = 10^8$ yr. Bottom panel: cumulative star formation before given time (blue line). The black hole mass growth $\Delta M_{\rm BH}$ (orange dashed line), which is synchronous with the starbursts, is also plotted for reference.

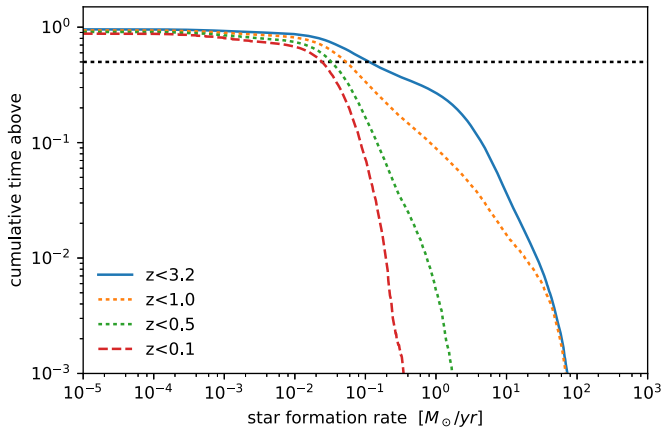

Figure 10. Duty cycle of star formation, i.e., percentage of cumulative time above given star formation rate. The horizon dotted line represents a fixed duty cycle of 50%.

Finally, we "feedback" this information to the radiative heating/cooling terms instantaneously, and to inner boundary conditions after a wind "travel" time $\sim R_{\rm in}/\bar{v}_w$. We assume that the AGN wind is of a bipolar configuration and weight the wind mass flux by $\cos^2(\theta)$. Provided the AGN luminosity and spectrum temperature, we are able to calculate the radiative heating/cooling *H–C*, and the radiation pressure due to both absorption and scattering are evaluated, respectively, as

$$(\nabla p_{\rm rad})_{\rm abs} = -\frac{H}{c}, \quad (\nabla p_{\rm rad})_{\rm es} = -\frac{\rho\kappa_{\rm es}}{c}\frac{L_{\rm BH}}{4\pi r^2}. \tag{33}$$

As usual, $\kappa_{\rm es}$ is the opacity due to electron scattering. In this way, we can simulate the galaxy evolution on a cosmological timescale of 12 Gyr with AGN feedback.

2.8. Initial and Boundary Conditions

To finalize the model setup, we specify the initial and boundary conditions in this section. For the initial conditions, we assume that there is some remnant ISM with 1/24 of the total stellar mass. The initial ISM is spread in the whole computational domain with the same density and velocity profiles as the stellar population, and the gas is thermalized to the local virial temperature, due to the stellar velocity dispersion and SN Ia heating.

At the (radial) inner and outer boundaries, we set the outflow boundary conditions (zero gradients; Stone & Norman 1992). The AGN wind feedback is implemented by injecting mass/momentum/energy accordingly into the innermost three layers of active (radial) cells just next to the inner boundary. The same technique is also used to implement the CGM infall at the outer boundary of our computational domain. To avoid artificial mass sources, we do not allow inflow at the outer boundary (other than the prescribed CGM infall) or outflow at the inner

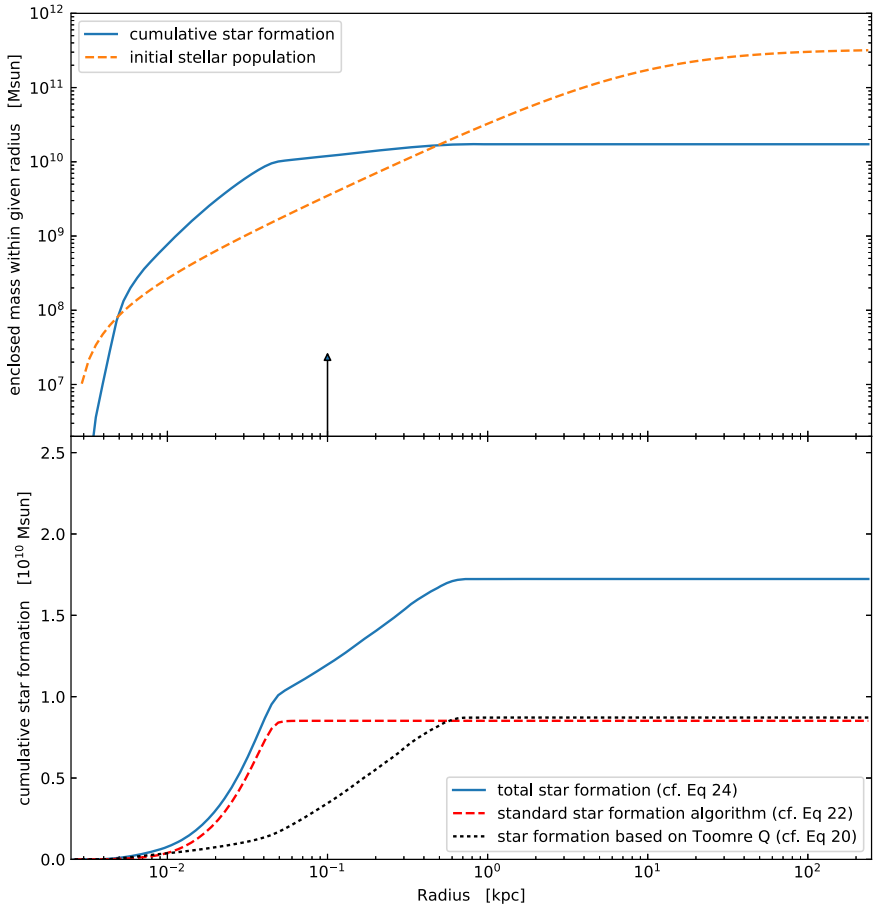

Figure 11. Total mass of the new (blue line) and old (orange dashed line) stellar populations enclosed by given radii. Most of the star formation occurs within $r \leqslant 3$ kpc. The mass of the newly formed stars is larger than the old stellar population around $r \leqslant 1$ kpc. The vertical arrow shows approximately the radius of influence of the black hole (∼100 pc). The inner boundary of the simulations is 2.5 pc.

boundary (aside from the designed BAL winds), and we set the axial reflecting boundary condition at the azimuthal boundaries.

3. Results

The physics ultimately driving the black hole feeding and feedback is the cooling flow (see Fabian 1994). As the ISM content is continuously enriched by the stellar mass loss (mainly from AGB stars) and by the CGM infall (mass accretion from the cosmic web), it is subject to strong radiative cooling. As the cooling rate is proportional to density squared, when the ISM density increases, the cooling timescale would eventually become comparable to or even shorter than the local dynamical timescale, and then a cooling flow is triggered.

As the ISM partially losses its thermal pressure, it will collapse onto the galaxy center and form a circumnuclear disk because of the angular momentum barrier. The dynamical timescale of the disk is much longer than the freefall timescale, so it allows mass to accumulate in the disk and to be cooled down catastrophically.

The cold disk would be extremely overdense, and it is subject to gravitational instability and to star formation. Meanwhile, the spiral waves, as a consequence of the gravitational instability, would also help to transfer angular momentum so as to allow mass to be accreted onto the galaxy center. It turns out that most of the cold gas would be consumed by star formation on its way to the supermassive black hole.

Finally, some of the gas would be accreted by the supermassive black hole, which lights up as an AGN (or even quasar). Consequently, strong AGN feedback is capable of altering all the processes above, driving galactic outflow, and regulating the black hole accretion itself by injecting huge amounts of energy and momentum (in terms of both radiation and wind) back into its host galaxy. The cooling flow will be quenched after large outbursts until another cycle starts over again.

3.1. Toomre Instability in the Cold Circumnuclear Disk

In Figure 5 we plot the ISM profiles of radial velocity, density, and temperature during an AGN/star formation burst. Note the bi-conical outflow in the middle vertical panels. We can clearly see some ripples induced by AGN feedback and a cold disk of size ∼1 kpc wiggling and sitting in the equatorial plane. More details of the cold disk are shown in Figure 6. We can see that the disk is cooled down to $\sim 10^4$ K (which simply hits the temperature floor of our numerical model). Such a temperature is far below the local virial temperature of $\sim 10^7$ K (see the orange line in the middle panel of Figure 6). It turns out that the cold disk is fully supported by rotation against the gravity; as shown in the top panel, the rotation profile of the disk fits perfectly with the analytical circular velocity derived from the total gravitational potential (see Equation (7)). The jump in pressure at the upper and lower surfaces of the disk is balanced by ram pressure of the infalling gas.

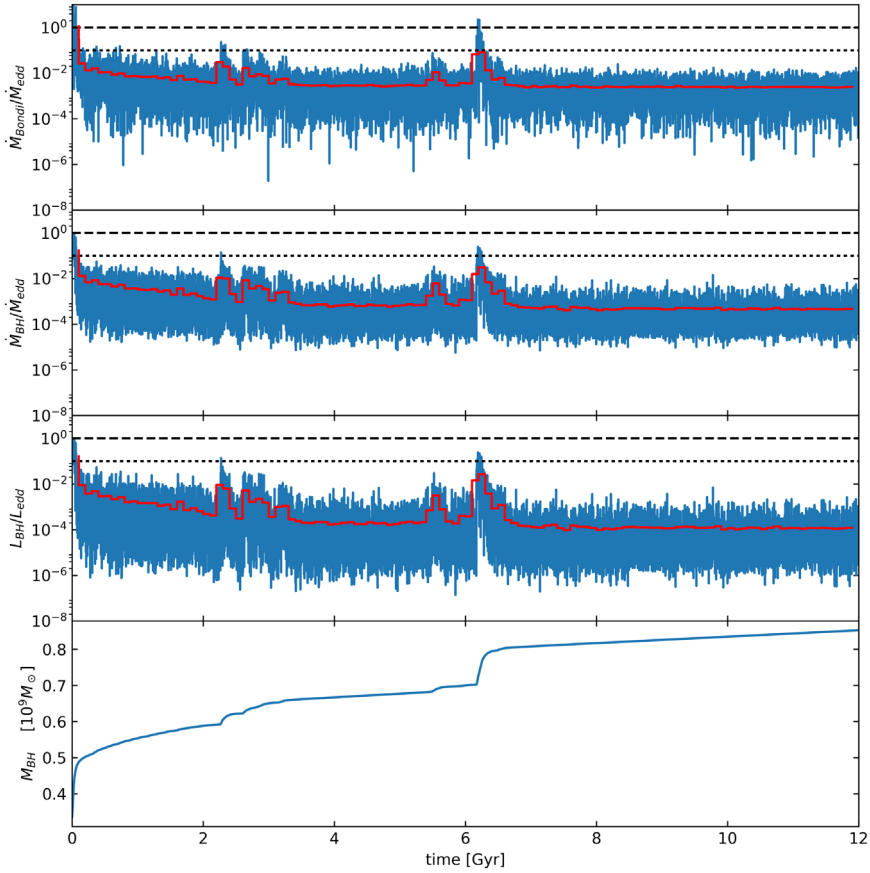

Figure 12. AGN activities and black hole mass growth. From top to bottom, the blue lines present, respectively, (1) the mass inflow at inner boundary, (2) the mass accretion rate onto the event horizon of the central supermassive black hole, (3) the bolometric luminosity of the AGN, and (4) the black hole mass. The red lines are the same as the blue lines, except that the data points are binned and averaged over equal time intervals of $\Delta t = 10^8$ yr. The mass flow rate and the AGN luminosity are normalized by the Eddington values (determined by the instantaneous black hole mass). The black dashed and dotted lines represent constant Eddington ratios of 1.0 and 0.1, respectively.

As the ISM cools down and continuously falls onto the disk (see Figure 3, left panel), its surface density increases. The disk can be finally overdense and becomes Toomre unstable in some individual rings, though the fraction of the unstable disk rings is extremely low (as shown in Figure 7, in which we plot the profiles of the Toomre Q parameter at a selection of representative times). As described in Sections 2.4 and 2.6, the Toomre instability is capable of transferring mass inward and will trigger star formation in the meantime (see Figure 8, top panel). As a result, the surface density decreases and the disk rings will be stabilized again. Because of the surface density threshold of the Toomre instability (Equation (13)), such processes are always bursty.

3.2. Star Formation History

All star formation occurs in the cold disk (as shown in the bottom panel of Figure 8). More precisely, most of the star formation takes place in individual disk rings, where it is subject to Toomre instability (as shown in the top panel of Figure 8). Hence, it is intrinsic that the new stars will be born in bursts. The star formation history is shown in Figure 9. In Figure 10 we analyze the duty cycle of star formation, i.e., percentage of cumulative time above the given star formation rate. In Figure 11, we show the enclosed mass of the cumulative star formation and compare it to the initial stellar mass profile.

We can see that most of the star formation occurs in the circumnuclear disk of a size $\leqslant 1$ kpc during the bursts in the early-stage evolution, which is in agreement with recent observations. For example, Tadaki et al. (2018) observed the starburst galaxy AzTEC-1 ($z = 4.3$) using ALMA. They found that a large fraction of stars are formed in the central 1 kpc region, plausibly in a gravitationally unstable gas disk. Such an observational phenomenon matches very well with the early bursts that we find in our simulations.

We note that the star formation rate in our simulation is actually low most of the time, especially in the late stage ($\leqslant 0.05\, M_\odot\, \mathrm{yr}^{-1}$), and it tends to be located on the very central ($r < 25$ pc) regions (Tan & Blackman 2005). The total star formation is roughly a few percent of the initial stellar mass. In Figure 11, we can also see that the new star mass could become larger than the initial stellar mass at $r \leqslant 1$ kpc, which could mildly alter the gravity profile in the central region.

However, for simplicity, we do not consider the gravity of the new stars in this paper. We leave it to our future work, in which we will consider a time-dependent galaxy dynamics model.

3.3. AGN Activities and Black Hole Mass Growth

Similar to star formation, the black hole accretion is also bursty, as it is driven by the same physical processes, i.e., the Toomre instability. In Figure 12, we plot the black hole accretion history; from the top to bottom panels, it shows the mass inflow rate via the inner boundary, the mass accretion rate down to the black hole event horizon, the consequent AGN

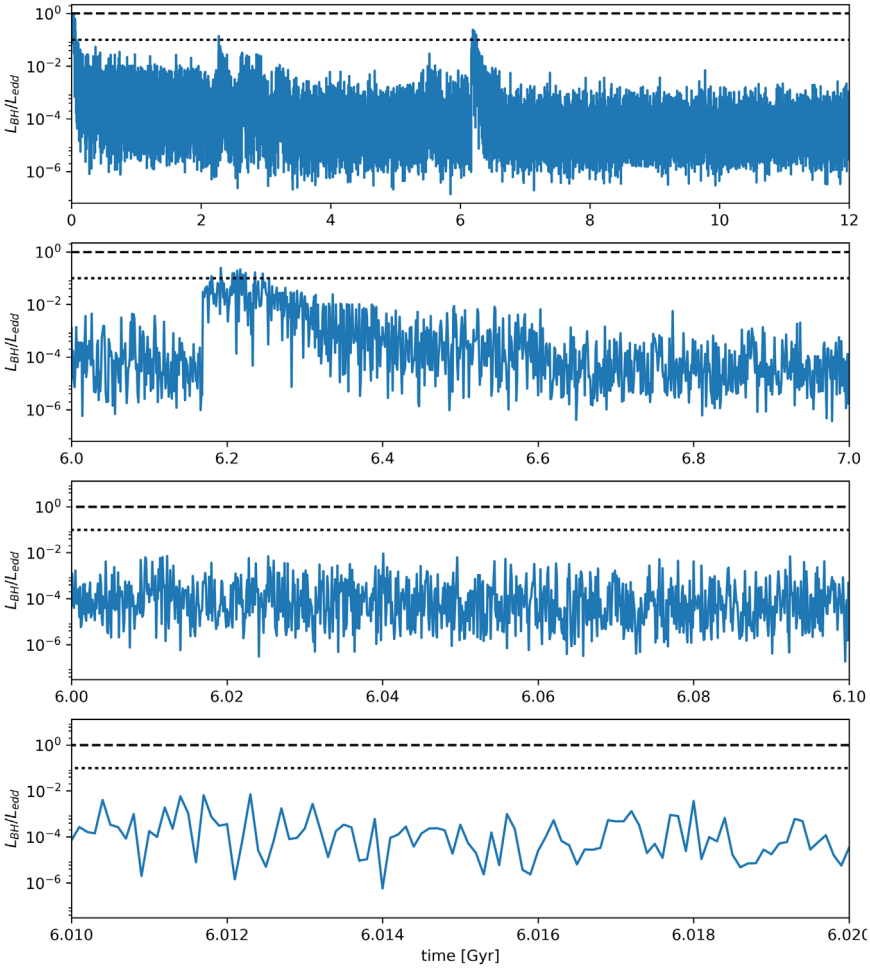

Figure 13. AGN bolometric luminosity as in Figure 12 (zoomed).

bolometric luminosity, and the black hole mass growth, respectively (more details of the AGN light curve can be found in Figure 13). In Figure 14 we analyze the AGN duty cycle in terms of cumulative energy/time when the AGN luminosity (the Eddington rate) is above given values. We can see that it agrees well with the Soltan argument, i.e., the AGN spends most of its lifetime at very low luminosity, while emitting most of its energy when it is at high luminosity (Soltan 1982).

3.4. Overall Mass Budget

We track the overall mass budget in Figure 15. As the mass source comes from (1) stellar mass loss, (2) CGM infall, and (3) the initial ISM content, we can see that most of the gas is expelled out of the galaxy, especially during the AGN bursts. One-quarter of the gas is consumed by star formation. Only a small fraction is accreted by the supermassive black hole. The rest remains in the galaxy, of which some is placed within the cold disk and the other is in the form of hot-phase ISM (which is capable of emitting X-rays). In the bottom panel, we can see that most of the mass inflow onto the galactic center (black line) is ejected as winds (orange line) and only a small fraction is finally accreted by the central black hole (blue line).

The spatial distribution of the remaining gas is shown in Figure 16. We can see that most of the hot ISM is located at the outskirts of the galaxy, where the density is too low to contribute to the X-ray luminosity. In Figure 17 we plot the time evolution of the ISM content, while in Figure 18 we plot the ISM X-ray luminosity. We see that the ISM X-ray luminosity lies in a reasonable range and agrees well with observations.

4. Effects of New Physics

In this section, we present the results of four control models, which are based on the fiducial run we showed previously, but with rotation, the Toomre instability, the α viscosity, or the hot-mode feedback turned off, respectively. In this way, we try to analyze the effects of the new physics we include in this paper. The statistical properties of the control models are summarized in Table 1.

In model C1, we turn off galaxy rotation by setting the rotation parameter k to be zero (see Equation (9)), i.e., it degenerates to the case of spherical symmetry. Of course, no cold gaseous disk is formed. Black hole feeding is mainly via accreting cold filaments. Significant black hole mass growth is allowed when compared to the fiducial model, while star formation decreases by a factor of 10^5. No obvious correlation between black hole growth and starburst has been found in this simulation (see also, e.g., Yuan et al. 2018).

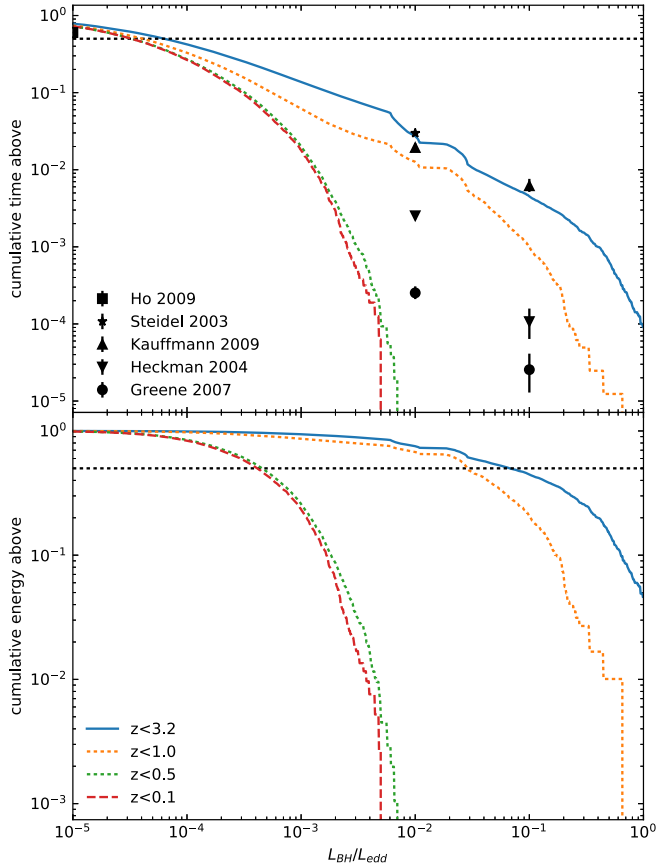

Figure 14. AGN duty cycle, i.e., percentage of cumulative time (top panel) and cumulative energy (bottom panel), above given Eddington ratio. The horizontal dashed lines represent a fixed duty cycle of 50%. The colored lines are the simulation results below a given redshift. The points are observational constraints. The squares, circles, and upward- and downward- pointing triangles are from Ho (2009), Greene & Ho (2007), Kauffmann & Heckman (2009), and Heckman et al. (2004), respectively, which are all compiled from low-redshift observations. The star is a constraint compiled from high-redshift observations by Steidel et al. (2003).

In model C2, we disable the effects of the Toomre instability (both angular momentum transfer and star formation). Black hole mass growth and star formation are significantly suppressed. The total mass of the circumnuclear disk keeps growing continuously; no (quasi-)steady state is found (note that there is still the α viscosity in the model setup). The cold gaseous disk is more massive and larger than observed in normal ellipticals.

In model C3, the α viscosity is turned off while all other physical processes are kept unchanged. We find fewer bursts of star formation and AGN activities in this run. At the late stage, when the cooling flow is weak, the circumnuclear disk tends to sit there without radial mass transport most of the time, as its surface density is not high enough to trigger the Toomre instability and thus the angular momentum transfer.

In model C4, the hot-mode feedback is disabled, i.e., both the AGN luminosity and the velocity of the nuclear wind are set to be zero when the AGN is in the hot mode. In this run, the low envelope of the black hole accretion rate, as a function of time, increases, and more black hole growth is via "low-level" accretion (see also Yoon et al. 2019, in preparation).

To sum up, star formation becomes much more efficient in consuming cold gas because of galaxy rotation, when compared to the case of spherical symmetry. The Toomre instability is responsible for transferring angular momentum in the circumnuclear disk, which is crucial for both the black hole feeding and star formation. Though the effects of α viscosity are weak, it is important to notice that it could still produce indirect effects on the "secular" evolution of the circumnuclear disk, i.e., continuously transferring angular momentum and allowing mass accretion onto the galaxy center, which may in turn induce the Toomre instability indirectly in the inner disk. Note that, with rotation, the fiducial model has the lowest rate of late star formation in best accord with observations (Ford & Bregman 2013).

5. Discussion and Conclusion

In this paper, we have improved our MACER (Massive AGN Controlled Ellipticals Resolved) code and performed 2.five-dimensional simulations on the ISM fluid dynamics in a rotating massive elliptical galaxy. The code is grid based and has high spatial resolution (parsecs in the inner regions), where the Bondi radius is readily resolved. The computational domain reaches to 250 kpc, which is large enough to enclose the whole massive elliptical galaxy. Both passive and active stellar evolution is considered, as are the mass sources from the outer and inner boundaries. By solving the hydrodynamics of the ISM with reasonable treatments of the thermal (radiative) and kinetic processes, we are able to resolve the cooling flow directly down to (and within) the Bondi radius; therefore, the mass accretion rate onto the supermassive black hole is determined self-consistently, which is critical to evaluate the AGN feedback, and the latter is also included in the code. The black hole mass growth is tracked during the cosmological evolution of its host galaxy, which makes it possible to study their coevolution in a single simulation (Fabian 2012; Kormendy & Ho 2013). Compared to our previous work (e.g., Gan et al. 2014; Yoon et al. 2018), the code has been improved comprehensively as outlined below.

We improve the galaxy modeling from a spherical configuration to allowing flattening and rotation (see also, e.g., Ciotti et al. 2017). The galaxy profile is extremely important in the numerical experiments, as it determines the characteristic temperature, velocity, and timescales of the whole system. In this paper, we use fully analytical axisymmetric models obtained by homeoidal expansion of the two-component spherical models (Ciotti & Ziaee Lorzad 2019, in preparation), which allows us to parameterize the galaxy morphology and its ordered rotation easily. As the stellar winds inherit the velocity of their host stars, the angular momentum of the ISM is determined self-consistently. The rotation profile of the ISM alters the fluid dynamics completely by impeding the gas from being accreted, leading to the formation of a circumnuclear disk, and favoring star formation in the disk. Similar behaviors can also be found in the SPH simulations by Eisenreich et al. (2017) , in which circumnuclear disks are commonly formed in the galaxy centers, and star formation occurs in those disks. As we have demonstrated, star formation is efficient enough to consume most of the cooled ISM before it could be accreted by the supermassive black hole (see also Li et al. 2018). Hence, one needs to consider angular momentum transfer to study the black hole feeding process, and the tough competition between angular momentum transfer and star formation ultimately determines the fate of the gas in the circumnuclear disk.

We propose a numerical algorithm to compute the angular momentum transfer due to the classic Toomre instability. Because of the angular momentum barrier, the ISM will

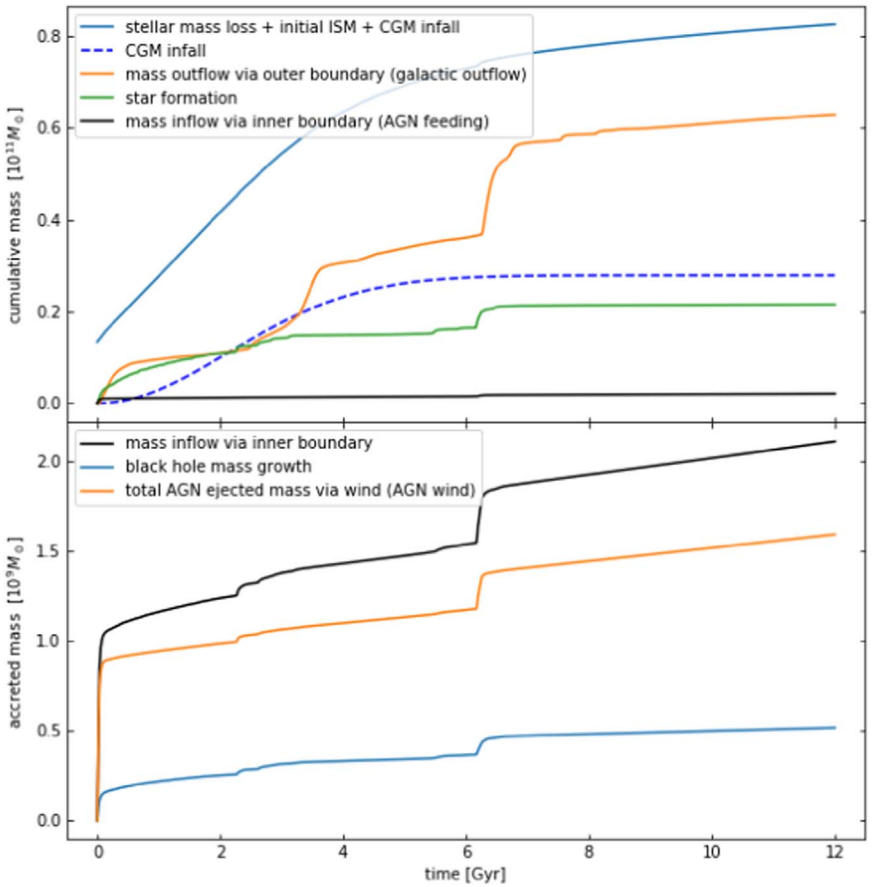

Figure 15. Mass budget, of the total ISM content (top panel) and of the black hole feeding (bottom panel), over the cosmological evolution. The top panel shows (1) the cumulative mass of the ISM sources (blue solid line; including the initial ISM remnant, the CGM infall [see the blue dashed line], and the stellar mass loss), (2) the cumulative mass of the galactic outflow that escaped from the outer boundary (which dominates the mass budget; orange line), (3) the cumulative mass of star formation (green line), and (4) the cumulative mass inflowing via the inner boundary (i.e., black hole feeding; black line). The bottom panel shows (1) the cumulative mass fed to the supermassive black hole (black line), (2) the black hole mass growth $\Delta M_{\rm BH}$ (blue line), and (3) the total mass injected by the AGN (via AGN wind feedback; orange line).

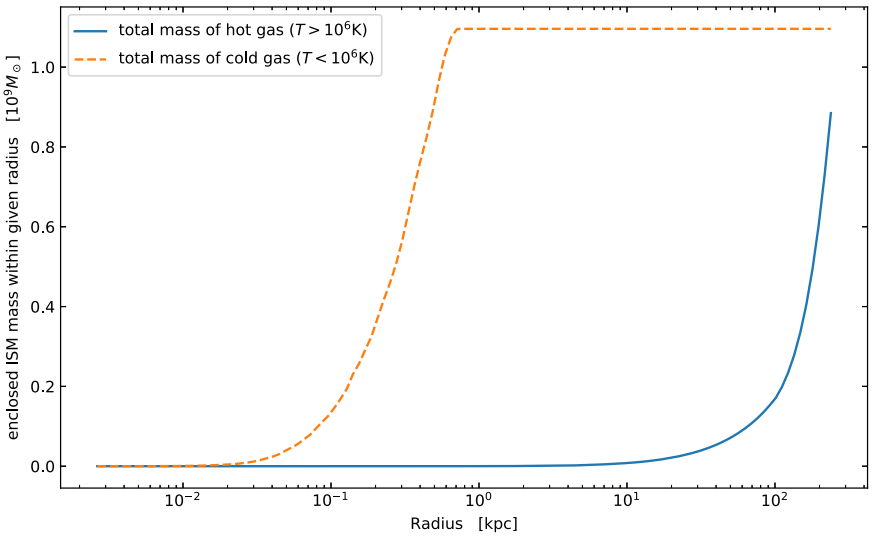

Figure 16. Total ISM mass remaining, in forms of hot gas ($T > 10^6$ K; blue line) and cold gas ($T < 10^6$ K; orange dashed line), at the end of the fiducial run. The cold gas is mainly in the circumnuclear disk within $r \leqslant 1$ kpc, while the hot gas is mainly in the galaxy outskirts (which minimally contributes to the total ISM X-ray luminosity because of its low density).

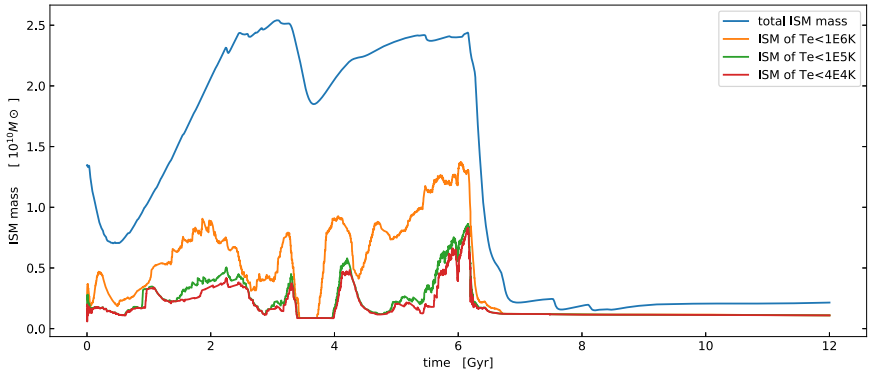

Figure 17. Time evolution of the cold-phase ISM. The rapid drops after the peaks are due to the Toomre instability, which drives both starbursts (see Figure 9) and strong AGN feedback (see Figure 12). Note that the cold gas with $T < 10^6$ K is mainly in the disk.

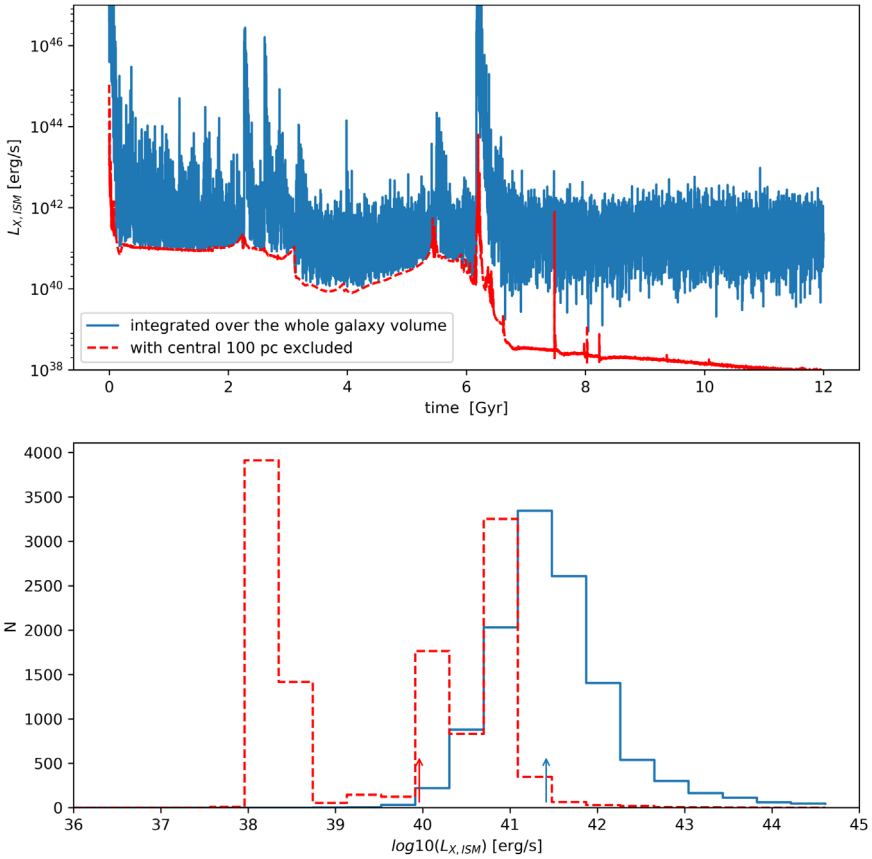

Figure 18. ISM X-ray luminosity in the band of 3–8 keV. The luminosity is calculated by integrating the frequency-dependent emissivity over the whole galaxy volume (blue lines; the blue vertical arrow in the bottom panel indicates its median value $L_{\rm X,ISM} = 2.5 \times 10^{41}$ erg s^{-1}). The red dashed lines show the results with the central 100 pc excluded (the red vertical arrow in the bottom panel indicates its median value $L_{\rm X,ISM} = 9.1 \times 10^{39}$ erg s^{-1}). The atomic data needed in the calculation are extracted from the ATOMDB code (version 3.0.9). In the bottom panel, we sample the ISM X-ray luminosity with equal time intervals of 0.01 Gyr and bin the data in logarithmic scale.

condense onto the circumnuclear disk and cool down further there. As a result, the disk surface density increases. The cold circumnuclear disk becomes gravitationally unstable when its surface density is higher than some critical value, and then spiral waves will develop because of the asymmetric gravitational torque, which are capable of transferring angular momentum outward and making mass inflowing possible. The Toomre Q parameter of the disk is evaluated instantaneously, and it is subject to the Toomre instability for those individual disk rings with $Q < 1$. We propose that the transfer rates of mass and angular momentum are proportional to $\Delta Q = \max(1 - Q, 0)$, and the timescale is comparable to the local orbital time. As mass accretion typically occurs when the circumnuclear disk is Toomre unstable (with some surface density threshold), the black hole feeding is always bursty. The cool, rotationally supported inner disk is also assumed to be MRI unstable and supports a weak α (=0.03) modulated viscosity that can transfer angular momentum in the absence of the Toomre instability.

We improve our standard star formation algorithm (based on local cooling and Jeans timescales) with low-temperature and high-density thresholds to mimic the conditions in star-forming

Table 1
Statistical Properties of the Modeling Galaxies

Model #	AGN Duty Cycle			$\Delta M_{\rm BH}$[d]	$\Delta M_{\rm w,AGN}$[e]	$\Delta M_{\rm w,Gal}$[f]	$\Delta M_{\star}^{+}$[g]	$\langle {\rm SFR} \rangle$[h]	Disk Size[i]
	$f_{E,l>0.1}$[a]	$l_{\rm median,E}$[b]	$l_{\rm median,t}$[c]	($M_\odot$)	($M_\odot$)	($M_\odot$)	($M_\odot$)	($M_\odot$ yr^{-1})	(kpc)
Fiducial	44.6%	6.7×10^{-2}	6.3×10^{-5}	5.17×10^{8}	1.59×10^{9}	6.28×10^{10}	2.15×10^{10}	3.5×10^{-2}	0.64
C1	51.1%	1.1×10^{-1}	8.0×10^{-5}	1.01×10^{9}	3.69×10^{9}	7.41×10^{10}	2.06×10^{5}	0.00	0.00
C2	6.06%	2.9×10^{-3}	9.2×10^{-5}	1.59×10^{8}	3.36×10^{8}	7.87×10^{9}	6.86×10^{9}	4.5×10^{-1}	1.52
C3	77.3%	2.8×10^{-1}	2.6×10^{-5}	4.21×10^{8}	2.23×10^{9}	5.32×10^{10}	2.98×10^{10}	1.4×10^{-1}	0.71
C4[j]	60.3%	1.6×10^{-1}	0.00	9.70×10^{8}	2.24×10^{9}	6.67×10^{10}	1.89×10^{10}	2.2×10^{-1}	0.86

Notes.
[a] The fraction of the cumulative AGN radiant energy when $l \equiv L_{\rm BH}/L_{\rm Edd} > 0.1$.
[b] The median AGN luminosity (in units of $L_{\rm Edd}$) above which an AGN emits half of its total radiant energy.
[c] The median AGN luminosity (in units of $L_{\rm Edd}$) above which an AGN spends half of the simulation time.
[d] Black hole mass growth.
[e] Total wind mass ejected by the AGN.
[f] Total wind mass expelled out of the host galaxy.
[g] Total star formation.
[h] The time-averaged star formation rate in the past 2 Gyr.
[i] The size of the circumnuclear disk at the end of the simulations.
[j] The experimental run C4 stops at $t = 7.3$ Gyr.

molecular clouds. For the star formation in the circumnuclear disk, we also propose an algorithm based on the Toomre Q parameter, i.e., the gravitation instability drives both angular momentum transfer and star formation with similar timescales. As we have demonstrated, the competition between angular momentum transfer and star formation is critical. On the other hand, it is natural in our model that AGN bursts usually accompany strong starbursts.

We use and modify the two-mode AGN feedback model as in Yuan et al. (2018). For the cold mode (high accretion rate; quasars), the implementation of AGN feedback is designed to match observed BAL winds and luminous output. For the hot mode (low accretion rate, low-luminosity AGNs), the properties of wind are usually hard to measure, so we propose the AGN feedback according to our knowledge gained from the theoretical studies (see Yuan et al. 2015 for details). The use of the two-mode scenario is that from both theoretical and observational studies we know that black hole accretion has two modes and in each mode the descriptions of AGN outputs are very different (see Yuan & Narayan 2014 for a review). The driving mechanisms of disk wind are also very different before/after the transition, especially in the hot mode, and the wind mass loading rate is usually much larger than the black hole accretion rate.

We consider various mass sources, including the CGM infall. It is important because the mass supply is comparable to that from stellar mass loss. With AGN/SN feedback, we can track the mass inflow/outflow at the galaxy outskirts. This also makes it possible for us to track the metal enrichment in/around the galaxy, which is reserved for our future work.

With the improved code above, we investigate the cosmological evolution of massive elliptical galaxies in detail. We find that the results agree reasonably well with observations (e.g., Davis et al. 2014, 2017):

1. Both AGN activity and star formation are primarily in central circumnuclear disks (in agreement with observations; van Dokkum & Franx 1995) and mainly driven by the Toomre instability, which are prone to be bursty, and they are associated with each other. Most of the gas on the disk is consumed by star formation before it can be accreted by the supermassive black hole.
2. The AGN duty cycle agrees well with the Soltan argument, i.e., the AGN spends most of its lifetime when it is in low luminosity, while emitting most of its energy when it is in high luminosity (Soltan 1982; Yu & Tremaine 2002);
3. The total star formation is roughly a few percent of the initial stellar mass occurring in the bursts that would be associated with the observed E+A phenomenon (Dressler & Gunn 1982). Most of the star formation occurs in a circumnuclear disk of size $\leqslant$1 kpc, which is in agreement with recent observations (e.g., Tadaki et al. 2018).
4. The ISM X-ray luminosity varies within a reasonable range and agrees well with observations.

In our current model setup, we do not include effects of dust, nor any background radiation from the stars or from X-ray binaries, which might be worthy of consideration in the future. An important process that we cannot easily include is late-epoch minor mergers. These significantly increase the mass of the high-mass ellipticals (see Oser et al. 2010) with the addition primarily of low-metallicity, old stars (van Dokkum et al. 2015) from accreted dwarf systems that puff up the outer stellar envelope (see van Dokkum et al. 2015; Greene et al. 2009) and increase the Sérsic index but do not greatly alter the structure within R_e. In the near future, we will perform detailed analysis on our simulation data and compare with observations. We will also simulate the evolution of the gas metallicity in/around the simulated galaxies by tracking the metal enrichment from the stellar/SN winds and metal dilution by the CGM infall.

We thank Ena Choi for sharing the CGM infall data. We thank Gregory S. Novak for sharing the first 2D version of the MACER code in 2011, which was using ZEUSMP/1.5. We thank Jeremy Goodman, James Stone, Silvia Pellegrini, Pieter van Dokkum, Nadia Zakamska, Luis Ho, Ena Choi, and Doosoo Yoon for useful discussions. Z.G. and F.Y. are supported in part by the National Key Research and Development Program of China (grant No. 2016YFA0400704), the Natural Science Foundation of

China (grants 11573051, 11633006, 11661161012), the Key Research Program of Frontier Sciences of CAS (No. QYZDJSSW-SYS008), the Natural Science Foundation of Shanghai (grant 18ZR1447200), and the Astronomical Big Data Joint Research Center, cofounded by the National Astronomical Observatories, Chinese Academy of Sciences, and the Alibaba Cloud. This work was done during Z.G.'s visit to the department of astronomy in Columbia University, which is supported by the Chinese Academy of Sciences via the visiting scholar program. We acknowledge computing resources from Columbia University's Shared Research Computing Facility project, which is supported by NIH Research Facility Improvement Grant 1G20RR030893-01, and associated funds from the New York State Empire State Development, Division of Science Technology and Innovation (NYSTAR) Contract C090171, both awarded 2010 April 15. Some of the simulations presented were performed with the computing resources made available via the Princeton Institute for Computational Science and Engineering.

Appendix A
Radiative Heating/Cooling under AGN Irradiation

In the energy equation, H and C are the radiative heating and cooling, respectively, including the contribution from AGN feedback. We use the formula from Sazonov et al. (2005),

$$H-C = n^2(S_{\rm comp} + S_{\rm brem} + S_{\rm line}), \tag{34}$$

which includes Compton heating/cooling $S_{\rm comp}$, bremsstrahlung cooling $S_{\rm brem}$, and line heating (photoionization)/cooling (recombination) $S_{\rm line}$ (see also Ciotti & Ostriker 2012). Here n is the H nuclear (number) density. The solar metal abundance is assumed in the calculations above.

Here we briefly introduce the radiative processes in Equation (34), which includes the contributions from both AGN irradiation and the local atomic processes (we refer the readers to Sazonov et al. 2005 for details):

1. Local bremsstrahlung cooling:

$$S_{\rm brem} = -3.8\times10^{-27}\sqrt{T}\quad {\rm erg\ cm^3\ s^{-1}}. \tag{35}$$

2. Comptonization. It could be either heating or cooling determined by the AGN radiation temperature $T_{\rm X}$ (given by Equation (32)):

$$S_{\rm comp} = 4.1\times10^{-35}(T_{\rm X}-T)\xi\quad {\rm erg\ cm^3\ s^{-1}}. \tag{36}$$

3. Photoionization heating $S_{\rm photo}$ and recombination cooling $S_{\rm recomb}$, i.e., $S_{\rm line} = S_{\rm photo} + S_{\rm recomb}$, where we use the fitting functions below:

$$S_{\rm recomb} = 10^{-23}\frac{a}{1+(\xi/\xi_0)^c}\quad {\rm erg\ cm^3\ s^{-1}} \tag{37}$$

$$S_{\rm photo} = 10^{-23}\frac{b\,(\xi/\xi_0)^c}{1+(\xi/\xi_0)^c}\quad {\rm erg\ cm^3\ s^{-1}} \tag{38}$$

and

$$a = -\frac{18}{e^{25(\log T-4.35)^2}} - \frac{80}{e^{5.5(\log T-5.2)^2}} - \frac{17}{e^{3.6(\log T-6.5)^2}}, \tag{39}$$

$$b = \frac{1.7\times10^4}{T^{0.7}}, \tag{40}$$

$$c = 1.1 - \frac{1.1}{e^{T/1.8\ 10^5}} + \frac{4\times10^{15}}{T^4}, \tag{41}$$

$$\xi_0 = \frac{1}{1.5/\sqrt{T} + 1.5\times10^{12}/\sqrt{T^5}} + \frac{4\times10^{10}}{T^2}\left[1+\frac{80}{e^{(T-10^4)/1.5\ 10^3}}\right]. \tag{42}$$

The effects of AGN irradiation involve Equations (36)–(38) via the ionization parameter ξ,

$$\xi \equiv \frac{L^{\rm eff}_{\rm BH,photo}(r)}{n\ r^2}. \tag{43}$$

To evaluate the local photoionization luminosity $L^{\rm eff}_{\rm BH,photo}(r)$, we integrate the radial radiation transfer equation below (Ciotti & Ostriker 2012):

$$\frac{dL^{\rm eff}_{\rm BH,photo}(r)}{dr} = -4\pi r^2 H, \tag{44}$$

where the radiative heating term H is ultimately determined by Equations (36)–(38), i.e.,

$$H = S_{\rm photo} + \max(S_{\rm comp}, 0). \tag{45}$$

Note that the formulae above are valid only when $T \geqslant 10^4$ K. Numerically, we set a temperature floor of 5×10^3 K for the self-consistency.

Appendix B
Stellar Feedback

Following Ciotti & Ostriker (2012) and Pellegrini (2012), we include both the passive stellar evolution (AGBs and SNe Ia) and the active stellar evolution (SNe II from the newly formed stellar population). It is well known that dying AGB stars eject winds (mass) and SNe eject huge amounts of energy, which are recycled by the galaxy and play an essential role in the galaxy evolution. The mass from AGB winds is far more than enough for feeding the supermassive black hole, and SNe are capable of heating up the ISM to the local viral temperature. Hence, those processes must be considered in the galaxy evolution modeling.

As in Section 2.6, we allow star formation in our simulations. In the newly formed stars, we assume that a considerable fraction (20%) of the newly formed star is high in mass ($M > 8\,M_\odot$) and will turn into an SN II in a timescale of $\tau_{\rm II} \simeq 2\times10^7$ yr. We parameterize the SN II feedback as follows:

$$\dot\rho_{\rm II} = \frac{\alpha_{\rm II}}{\tau_{\rm II}}\int_0^t \dot\rho^+_\star(t')\cdot e^{-\frac{t-t'}{\tau_{\rm II}}}dt',$$
$$\dot E_{\rm II} = \eta_{\rm SN}\cdot\frac{\epsilon_{\rm II}c^2}{\tau_{\rm II}}\int_0^t \dot\rho^+_\star(t')\cdot e^{-\frac{t-t'}{\tau_{\rm II}}}dt', \tag{46}$$

where $\alpha_{\rm II}$ is the ratio of SN II mass ejecta to the total star formation mass, and $\epsilon_{\rm II}$ is the SN II energy efficiency. Following Ciotti & Ostriker (2012), we assume that (1) the newly formed stars have a Salpeter IMF; (2) each massive star leaves a remnant of $1.4\,M_\odot$; and (3) each SN II explosion releases energy of 10^{51} erg. We could get $\alpha_{\rm II} = 0.2$ and $\epsilon_{\rm II} = 1.9\times10^{-5}$.

We parameterize the SN Ia rate as

$$R_{\rm SN}(t) = 0.32 \times 10^{-12} h^2 \frac{L_{\rm B}}{L_{\rm B\odot}} \times \left(\frac{t}{13.7{\rm Gyr}}\right)^{-1.1} {\rm yr}^{-1}, \quad (47)$$

where $h = H_0/100$ km s^{-1} Mpc^{-1}. We assume that each SN Ia event releases $\Delta E_{\rm I} = 10^{51}$ erg of energy and ejects $\Delta M_{\rm I} = 1.4\,M_\odot$ of material into the ISM (i.e., the energy efficiency $\epsilon_{\rm I} \equiv \Delta E_{\rm I}/\Delta M_{\rm I} c^2 = 3.996 \times 10^{-4}$). Similarly, we calculate the mass and energy injection of unit volume as

$$\dot{\rho}_{\rm I} = \Delta M_{\rm I} \frac{R_{\rm SN}}{M_\star} \rho_\star, \quad \dot{E}_{\rm I} = \eta_{\rm SN} \cdot \epsilon_{\rm I}\, \dot{\rho}_{\rm I} c^2, \quad (48)$$

where $\eta_{\rm SN}$ in the equation above (and in Equation (46)) is the SN energy dissipation efficiency to the ISM. And we need the mass-to-light ratio $\Gamma \equiv M_\star/L_B$ to normalize Equation (47). We usually set $\eta_{\rm SN} = 0.85$ and $\Gamma = 5.8$ in solar units.

Following Ciotti et al. (1991), we evaluate the stellar mass loss according to the stellar evolution theory, and we assume a Salpeter IMF (see also Ciotti & Ostriker 2012; Pellegrini 2012),

$$\dot{M}_\star = {\rm IMF}(M_{\rm TO}) |\dot{M}_{\rm TO}| \Delta M, \quad (49)$$

where the turnoff mass $M_{\rm TO}$ and its mass loss ΔM (in units of $M_\odot$) at time t (in units of Gyr) are, respectively,

$$\log M_{\rm TO} = 0.0588 (\log t)^2 - 0.3336 \log t + 0.2418, \quad (50)$$

$$\Delta M = \begin{cases} 0.945\, M_{\rm TO} - 0.503, & M_{\rm TO} < 9, \\ M_{\rm TO} - 1.4, & M_{\rm TO} \geqslant 9. \end{cases} \quad (51)$$

Then, we calculate the local stellar mass loss $\dot{\rho}_\star$ by scaling Equation (49) with the stellar mass density $\rho_\star$ (see Equation (4)) and evaluate the thermalization of the stellar mass loss according to its velocity dissipation (Equation (11); see also Ciotti et al. 2017), i.e.,

$$\dot{\rho}_\star = \rho_\star \cdot \dot{M}_\star/M_\star \quad \dot{E}_S = \frac{1}{2}(\dot{\rho}_\star + \dot{\rho}_I + \dot{\rho}_{II}) \cdot [{\rm Tr}(\sigma^2) + \|\boldsymbol{v} - v_{\varphi\star}\boldsymbol{e}_\varphi\|^2]. \quad (52)$$

In the equation above, we assumed that the stellar mass loss inherits the ordered rotation velocity of its host stars (see Equation (9)). Finally, we inject momentum associated with the stellar mass loss accordingly,

$$\dot{m}_S = (\dot{\rho}_\star + \dot{\rho}_I + \dot{\rho}_{II}) \cdot v_{\varphi\star}. \quad (53)$$

ORCID iDs

Zhaoming Gan https://orcid.org/0000-0003-3886-0383
Luca Ciotti https://orcid.org/0000-0002-5708-5274
Jeremiah P. Ostriker https://orcid.org/0000-0002-6405-9904
Feng Yuan https://orcid.org/0000-0003-3564-6437

References

Arav, N., Li, Z.-Y., & Begelman, M. C. 1994, ApJ, 432, 62
Arav, N., Moe, M., Costantini, E., et al. 2008, ApJ, 681, 954
Balbus, S. A., & Hawley, J. F. 1998, RvMP, 70, 1
Boizelle, B. D., Barth, A. J., Darling, J., et al. 2017, ApJ, 845, 170
Booth, C. M., & Schaye, J. 2009, MNRAS, 398, 53
Brennan, R., Choi, E., Somerville, R. S., et al. 2018, ApJ, 860, 14
Cattaneo, A., & Teyssier, R. 2007, MNRAS, 376, 1547
Choi, E., Ostriker, J. P., Naab, T., et al. 2017, ApJ, 844, 31
Choi, E., Ostriker, J. P., Naab, T., & Johansson, P. H. 2012, ApJ, 754, 125
Ciotti, L., & Bertin, G. 2005, A&A, 437, 419
Ciotti, L., D'Ercole, A., Pellegrini, S., & Renzini, A. 1991, ApJ, 376, 380
Ciotti, L., & Ostriker, J. P. 1997, ApJL, 487, L105
Ciotti, L., & Ostriker, J. P. 2007, ApJ, 665, 1038
Ciotti, L., & Ostriker, J. P. 2012, ASSL, 378, 83
Ciotti, L., & Pellegrini, S. 1996, MNRAS, 279, 240
Ciotti, L., Pellegrini, S., Negri, A., & Ostriker, J. P. 2017, ApJ, 835, 15
Ciotti, L., & Ziaee Lorzad, A. 2018, MNRAS, 473, 5476
Crain, R. A., Schaye, J., Bower, R. G., et al. 2015, MNRAS, 450, 1937
Davis, T. A., Alatalo, K., Sarzi, M., et al. 2011, MNRAS, 417, 882
Davis, T. A., Bureau, M., Onishi, K., et al. 2017, MNRAS, 468, 4675
Davis, T. A., Young, L. M., Crocker, A. F., et al. 2014, MNRAS, 444, 3427
Debuhr, J., Quataert, E., & Ma, C.-P. 2011, MNRAS, 412, 1341
Di Matteo, T., Springel, V., & Hernquist, L. 2005, Natur, 433, 604
Dressler, A., & Gunn, J. E. 1982, ApJ, 263, 533
Drory, N., Bundy, K., Leauthaud, A., et al. 2009, ApJ, 707, 1595
Dubois, Y., Devriendt, J., Slyz, A., & Teyssier, R. 2010, MNRAS, 409, 985
Dubois, Y., Gavazzi, R., Peirani, S., & Silk, J. 2013, MNRAS, 433, 3297
Eisenreich, M., Naab, T., Choi, E., Ostriker, J. P., & Emsellem, E. 2017, MNRAS, 468, 751
Fabian, A. C. 1994, ARA&A, 32, 277
Fabian, A. C. 2012, ARA&A, 50, 455
Fabian, A. C., Walker, S. A., Russell, H. R., et al. 2017, MNRAS, 464, L1
Ford, H. A., & Bregman, J. N. 2013, ApJ, 770, 137
Gan, Z., Yuan, F., Ostriker, J. P., Ciotti, L., & Novak, G. S. 2014, ApJ, 789, 150
Gaspari, M., Ruszkowski, M., & Sharma, P. 2012, ApJ, 746, 94
Greene, J. E., & Ho, L. C. 2007, ApJ, 667, 131
Greene, J. E., Zakamska, N. L., Liu, X., Barth, A. J., & Ho, L. C. 2009, ApJ, 702, 441
Guo, F., & Oh, S. P. 2008, MNRAS, 384, 251
Heckman, T. M., Kauffmann, G., Brinchmann, J., et al. 2004, ApJ, 613, 109
Hirschmann, M., Dolag, K., Saro, A., et al. 2014, MNRAS, 442, 2304
Hitomi Collaboration 2016, Natur, 535, 117
Ho, L. C. 2009, ApJ, 699, 638
Hopkins, P. F., & Quataert, E. 2010, MNRAS, 407, 1529
Hopkins, P. F., & Quataert, E. 2011, MNRAS, 415, 1027
Hopkins, P. F., Wetzel, A., Kereš, D., et al. 2018, MNRAS, 480, 800
Jaffe, W. 1983, MNRAS, 202, 995
Kauffmann, G., & Heckman, T. M. 2009, MNRAS, 397, 135
Kormendy, J., & Ho, L. C. 2013, ARA&A, 51, 511
Li, J., Ostriker, J., & Sunyaev, R. 2013, ApJ, 767, 105
Li, Y.-P., Yuan, F., Mo, H., et al. 2018, ApJ, 866, 70
Lodato, G. 2008, NewAR, 52, 21
Magorrian, J., Tremaine, S., Richstone, D., et al. 1998, AJ, 115, 2285
Naab, T., Johansson, P. H., Ostriker, J. P., & Efstathiou, G. 2007, ApJ, 658, 710
Naab, T., & Ostriker, J. P. 2017, ARA&A, 55, 59
Narayan, R., SÄdowski, A., Penna, R. F., & Kulkarni, A. K. 2012, MNRAS, 426, 3241
Negri, A., Ciotti, L., & Pellegrini, S. 2014a, MNRAS, 439, 823
Negri, A., Pellegrini, S., & Ciotti, L. 2015, MNRAS, 451, 1212
Negri, A., Posacki, S., Pellegrini, S., & Ciotti, L. 2014b, MNRAS, 445, 1351
Nesvadba, N. P. H., De Breuck, C., Lehnert, M. D., Best, P. N., & Collet, C. 2017, A&A, 599, A123
Nesvadba, N. P. H., Lehnert, M. D., De Breuck, C., Gilbert, A., & van Breugel, W. 2007, A&A, 475, 145
Nesvadba, N. P. H., Lehnert, M. D., Eisenhauer, F., et al. 2006, ApJ, 650, 693
Novak, G. S., Ostriker, J. P., & Ciotti, L. 2011, ApJ, 737, 26
Oser, L., Ostriker, J. P., Naab, T., Johansson, P. H., & Burkert, A. 2010, ApJ, 725, 2312
Ostriker, J. P., Choi, E., Ciotti, L., Novak, G. S., & Proga, D. 2010, ApJ, 722, 642
Pellegrini, S. 2012, ASSL, 378, 21
Pellegrini, S., Ciotti, L., Negri, A., & Ostriker, J. P. 2018, ApJ, 856, 115
Posacki, S., Pellegrini, S., & Ciotti, L. 2013, MNRAS, 433, 2259
Renzini, A., Ciotti, L., D'Ercole, A., & Pellegrini, S. 1993, ApJ, 419, 52
Salomé, P., Combes, F., Edge, A. C., et al. 2006, A&A, 454, 437
Sarzi, M., Falcón-Barroso, J., Davies, R. L., et al. 2006, MNRAS, 366, 1151
Satoh, C. 1980, PASJ, 32, 41

Sazonov, S. Y., Ostriker, J. P., Ciotti, L., & Sunyaev, R. A. 2005, MNRAS, 358, 168
Shakura, N. I., & Sunyaev, R. A. 1973, A&A, 24, 337
Sijacki, D., Vogelsberger, M., Genel, S., et al. 2015, MNRAS, 452, 575
Soltan, A. 1982, MNRAS, 200, 115
Somerville, R. S., & Davé, R. 2015, ARA&A, 53, 51
Springel, V., Di Matteo, T., & Hernquist, L. 2005, MNRAS, 361, 776
Steidel, C. C., Adelberger, K. L., Shapley, A. E., et al. 2003, ApJ, 592, 728
Stone, J. M., Gardiner, T. A., Teuben, P., Hawley, J. F., & Simon, J. B. 2008, ApJS, 178, 137
Stone, J. M., & Norman, M. L. 1992, ApJS, 80, 753
Stone, J. M., Pringle, J. E., & Begelman, M. C. 1999, MNRAS, 310, 1002
Tadaki, K., Iono, D., Yun, M. S., et al. 2018, Natur, 560, 613
Takasao, S., Tomida, K., Iwasaki, K., & Suzuki, T. K. 2018, ApJ, 857, 4
Tan, J. C., & Blackman, E. G. 2005, MNRAS, 362, 983
Toomre, A. 1964, ApJ, 139, 1217
Tortora, C., Antonuccio-Delogu, V., Kaviraj, S., et al. 2009, MNRAS, 396, 61
Tremmel, M., Quinn, T. R., Ricarte, A., et al. 2019, MNRAS, 483, 3336
van Dokkum, P. G., & Franx, M. 1995, AJ, 110, 2027
van Dokkum, P. G., Nelson, E. J., Franx, M., et al. 2015, ApJ, 813, 23
Wagner, A. Y., Bicknell, G. V., & Umemura, M. 2012, ApJ, 757, 136
Weinberger, R., Springel, V., Pakmor, R., et al. 2018, MNRAS, 479, 4056
Xie, F.-G., & Yuan, F. 2012, MNRAS, 427, 1580
Xie, F.-G., Yuan, F., & Ho, L. C. 2017, ApJ, 844, 42
Yang, H.-Y. K., & Reynolds, C. S. 2016, ApJ, 829, 90
Yoon, D., Yuan, F., Gan, Z., et al. 2018, ApJ, 864, 6
Yu, Q., & Tremaine, S. 2002, MNRAS, 335, 965
Yuan, F., Bu, D., & Wu, M. 2012, ApJ, 761, 130
Yuan, F., Gan, Z., Narayan, R., et al. 2015, ApJ, 804, 101
Yuan, F., & Narayan, R. 2014, ARA&A, 52, 529
Yuan, F., Yoon, D., Li, Y., et al. 2018, ApJ, 857, 121
Zhu, Z., & Stone, J. M. 2018, ApJ, 857, 34
Zhuravleva, I., Churazov, E., Arévalo, P., et al. 2016, MNRAS, 458, 2902